

Peer review status:

This is a non-peer-reviewed preprint submitted to EarthArXiv.

### Abstract

A total of integrated geophysical and hydrochemical investigations were conducted to characterize groundwater salinization in the western Nile Delta, Egypt. Twenty-five time-domain electromagnetic (TDEM) soundings and 30 water samples (depths 5-167 m) were used together with borehole logs and temporal comparison to 2012 datasets. One-dimensional TDEM inversion and 3-D resistivity modeling delineate six geoelectric units: a thin weathered layer (2-20 m), a shallow clayey-sand aquifer (10–40 m), a main sand aquifer (30–120 m), confining clay layers, sandy-clay horizons, and a deep conductive body interpreted as seawater intrusion. Spatial hydrochemical mapping shows TDS ranging from 388 to 9,610 mg·L<sup>-1</sup> in the shallow aquifer and 553 to 9,150 mg·L<sup>-1</sup> in the main aguifer, with nitrate hotspots (up to 948 mg·L<sup>-1</sup>) associated with agricultural recharge. Temporal comparison (2012–2023) reveals intensification of salinity in the north (deep saline plume, Cl up to 3,000 mg·L and progressive northward encroachment. Integration of resistivity and chemistry confirms an inverse resistivity-TDS relationship, though low resistivity in some areas reflects clay rather than salinity. This study recommends targeted reductions in pumping in the northern sector, artificial recharge and hydraulic barriers where feasible, regulation of fertilizer use in the central sectors, denser geophysical surveys, and a continuous chemical monitoring program. These findings provide a replicable framework to assess salinization in deltaic, semi-arid aquifers and to guide local water-resource management.

# Keywords

TDEM; Hydrogeochemistry; Seawater intrusion; West Nile Delta; Groundwater salinization; Egypt

# 1. Introduction

Groundwater represents the primary source of freshwater for domestic, agricultural, and industrial uses in many arid and semi-arid regions, including northern Egypt. In the western Nile Delta, the rapid expansion of agricultural reclamation projects, population growth, and intensified groundwater abstraction have placed considerable pressure on aquifer systems. These stresses have altered the natural hydraulic balance, leading to progressive salinization driven by seawater intrusion, vertical leakage between aquifers, and contamination from agricultural return flows. The resulting degradation in groundwater quality threatens the sustainability of local water resources and poses significant challenges for agricultural productivity and rural livelihoods.

The study area lies within the western portion of the Nile Delta, which is characterized by complex interactions among geomorphology, sedimentary facies, and structural controls. The lateral and vertical distribution of clay lenses strongly influences groundwater flow patterns, recharge conditions, and the vulnerability of aquifers to salinization ((Abd-Allah et al. 2012); Salem & El-Bayumy 2016; Hasan et al. 2023). Moreover, the region is structurally situated within the Marmarican Homocline, where minor faulting and subtle flexures modify aquifer geometry and create preferential pathways that may either enhance or restrict saline migration. As a result, the strata dipped gently northward and eastward, reflecting the influence of the structural elements associated with the Taphro-geosynclinal basin of the Nile Delta((Shata et al. 1978)). Understanding the geometry and hydraulic behavior of these aquifer systems is therefore critical for diagnosing the mechanisms of salinity evolution and formulating sustainable groundwater management strategies

Groundwater salinization in the Nile Delta, Egypt, is driven by a combination of natural and anthropogenic processes, including seawater intrusion, irrigation return flow, evaporite dissolution, and cation exchange, all of which collectively contribute to the deterioration of aquifer quality (Kotb et al. 2000; Williams 2001; Moursy et al. 2025). Seawater intrusion progresses inland when groundwater abstraction exceeds natural recharge, particularly in the northern Delta, where excessive pumping lowers the freshwater hydraulic head and allows saline water to migrate landward (Sherif and Singh 1997; ElMahmoudi et al. 2020). Agricultural irrigation practices further intensify salinization by returning dissolved salts and nutrients to the shallow aquifer system, especially under high evapotranspiration conditions typical of arid environments (El Bastawesy et al. 2016; El-Hassanin et al. 2016). Additionally,

evaporite dissolution and cation exchange reactions alter groundwater ionic composition along flow paths, particularly within Miocene aquifers distributed across the eastern and western Delta margins (Sallouma and Gomaa 1997; Van Engelen et al. 2018). Effective mitigation requires an integrated groundwater management framework. Regulating abstraction to align with sustainable recharge rates can reduce salinity advancement by up to 40% in vulnerable coastal sectors, whereas Managed Aquifer Recharge (MAR) techniques, such as infiltration basins or the controlled use of treated wastewater, can create hydraulic barriers that limit seawater encroachment (El-Hassanin et al. 2016; Negm et al. 2018) Therefore, disentangling the relative influence of these interacting processes necessitates a combined hydrogeochemical and geophysical investigative approach.

In coastal and deltaic aquifer systems, including the Western Nile Delta, several investigations have shown that seawater intrusion, excessive groundwater abstraction, agricultural return flow, and leakage through semi-confining layers are the primary drivers of groundwater degradation (Awad et al. 2022; Aboukota et al. 2024). Over-pumping reduces hydraulic heads and promotes landward migration of saline groundwater, while intensive irrigation contributes to elevated nitrate and dissolved salt concentrations, further compromising water quality (Zhang et al. 2024) These interacting natural (marine and lithologic) and anthropogenic (agricultural and pumping) factors collectively shape the hydrogeochemical conditions observed in the present study area, where vertical leakage, salinity mixing, and contamination from surface activities play critical roles in groundwater salinization.

Recent hydro-geophysical investigations have provided valuable insights into the subsurface characteristics of the West Nile Delta aquifers(Gad et al. 2016; Ibraheem et al. 2016; Araffa and Soliman 2019; Mashaal et al. 2020; Mansour et al. 2023; Abuzaid et al. 2024; Ali et al. 2024; El-Agha et al. 2024; Abdalsalam et al. 2025; Araffa et al. 2025; Elbeih et al. 2025; Khalifa and Gemail 2025). These studies have employed a range of geophysical techniques, including Time Domain Electromagnetic (TDEM), Vertical Electrical Sounding (VES), and DC resistivity, Very low Frequency (VLF) to delineate subsurface structures and assess the hydrogeological regime. The findings indicate that the shallow Pleistocene aquifer, primarily composed of gravelly to clayey sand deposits, plays a critical role in the region's groundwater potential. Moreover, significant variations in water quality have been observed, distinguishing between brackish groundwater in some zones and relatively fresh water in deeper layers.

Electromagnetic (EM) methods, notably Time-Domain Electromagnetic (TDEM) soundings, offer critical insights into subsurface resistivity distributions, effectively delineating freshwater and saline groundwater zones in the West Nile Delta (Krivochieva and Chouteau 2003; Ziadi et al. 2017; Francés et al. 2024) TDEM data enable the assessment of aquifer conditions, confined or unconfined, by mapping the geometry of water-bearing units, including their thickness, lateral extent, and depths to upper and lower boundaries (Abdalsalam et al. 2025; Araffa et al. 2025). TDEM is particularly adept at identifying conductive saline bodies and clay-rich confining layers that control groundwater flow (Khalifa and Gemail 2025). However, low resistivity can reflect either high salinity or increased clay content, necessitating integration with hydrochemical analyses to resolve ambiguities in lithological versus quality-driven variations (Abuzaid et al. 2024; El-Agha et al. 2024). Also, resolving finer features requires denser station spacing, integration with Electrical Resistivity Tomography (ERT), and correlation with borehole logs.

Hydro-geochemical processes have been widely investigated to understand groundwater evolution, the origins of salinity, and the mechanisms driving water-quality deterioration across different climatic and hydrogeological settings. In arid and semi-arid regions, notably in northern Egypt, previous work has highlighted the dominant roles of evaporation, evapotranspiration, and mineral dissolution in concentrating dissolved ions and controlling groundwater chemistry (Joshi et al. 2009; Wu et al. 2013; Mohammed et al. 2022; Nosair et al. 2025). By contrast, temperate and tropical regions studies emphasize the growing influence of anthropogenic pressures, irrigation return flow, fertilizer leaching, and industrial discharge, which accelerate salinization and alter ionic compositions (Shin et al. 2022; Amiri et al. 2023). The Water Quality Index (WQI) is now commonly applied, together with spatial mapping, to assess groundwater suitability for drinking and irrigation and to reveal patterns of spatial variability (Kumar and Maurya 2023; Alzahrani et al. 2025).

This study integrates Time-Domain Electromagnetic (TDEM) inversion results, three-dimensional resistivity modeling, hydrochemical analyses, and temporal comparisons with earlier datasets to characterize groundwater salinization patterns in the central part of Beheira Governorate, northern Egypt. The investigated area (Figure 1), covering approximately 100 km², extends along the Nubaria Canal between Damanhour, El Delengat, and Housh Eissa cities, and is intersected by the Alexandria agricultural road. It is characterized by intensive agricultural activities supported by surface irrigation from the canal and groundwater abstraction from underlying aquifers. The main objectives of this study are to: (1) delineate the

geometry and spatial variability of the existing aquifers, (2) map the distribution and intensity of saline intrusion and identify its controlling structural and lithological factors, and (3) evaluate the hydrochemical evolution of groundwater to distinguish between natural and anthropogenic sources of salinity. This study establishes a comprehensive framework for assessing groundwater vulnerability in semi-arid aquifer systems and provides a replicable approach applicable to similar environments worldwide.

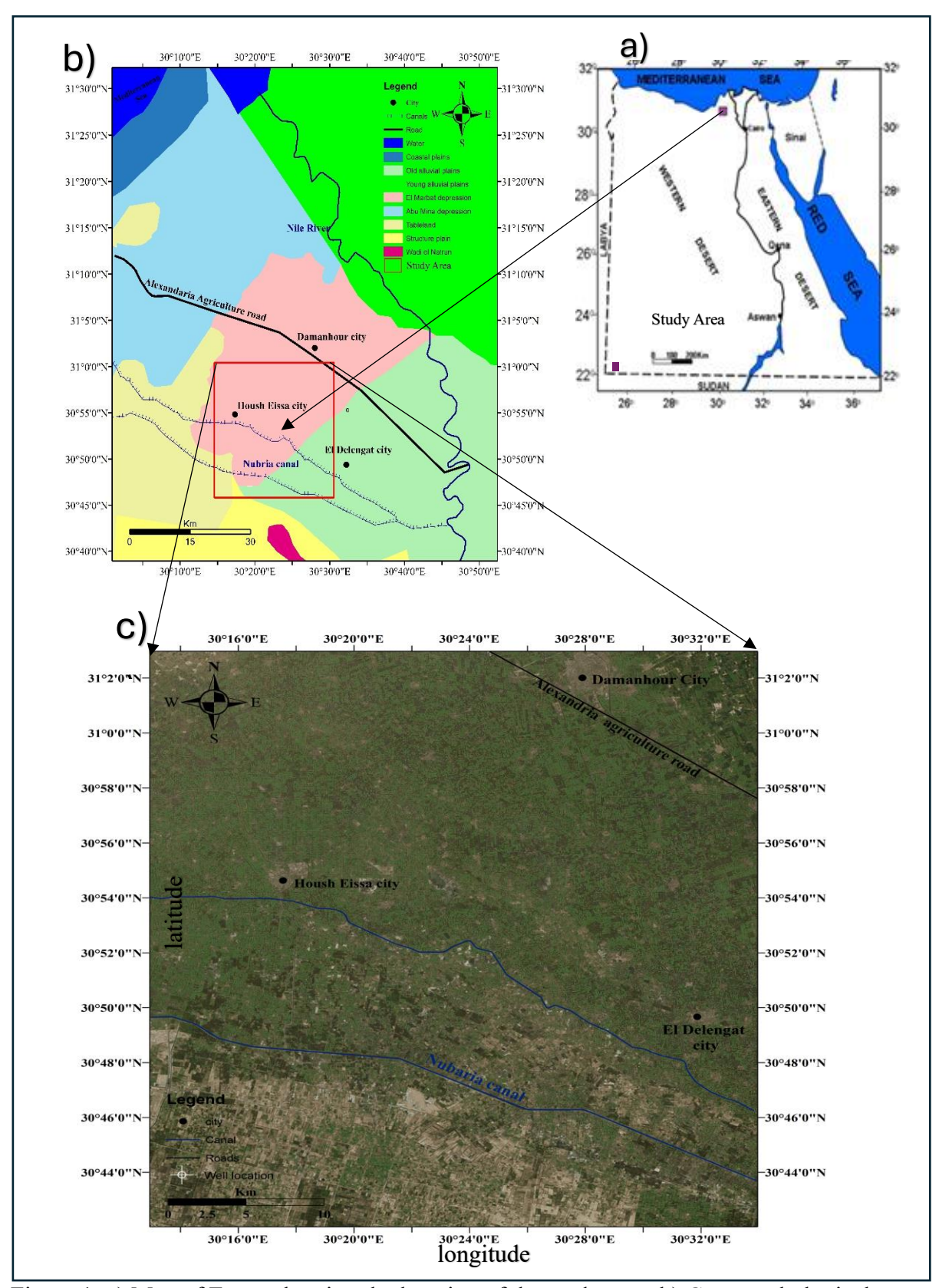


Figure 1: a) Map of Egypt showing the location of the study area. b) Geomorphological map of the West Nile Delta region. c) Satellite image of the study area (adapted from Google Earth Pro, 2025).

# 2. Geological and Geomorphological Setting

# 2.1 Geomorphology and Land Use

Geomorphologically, the study area lies within Egypt's West Nile Delta region and has been described by several authors (Sandford and Arkell 1939; Said 1962a; Shata et al. 1978; Embaby 2003a). It is situated within two distinct geomorphological units: the Old Alluvial Plain and the El-Marbat Depression (Figure 1b). The Old Alluvial Plain covers the southern and western sectors of the area, characterized by a gently rolling surface that slopes northward and northeastward. It is primarily composed of sandy and gravelly deposits. The El-Marbat Depression represents a structural low formed by NW–SE trending faults associated with the unstable northern shelf of the Western Desert (Abd-Allah et al. 2012). Continued tectonic subsidence, combined with the accumulation of Nile-derived sediments, particularly during the Pleistocene and Holocene, has resulted in the deposition of thick sequences of sand, gravel, and clay (Pennington et al. 2017).

Over the past few decades, remote sensing and Landsat imagery have revealed significant changes in land use across the region (Figure 2). Large tracts of the old deltaic plain have been reclaimed for agriculture since the 1980s (USGS 1984), transforming formerly desert lands into cultivated fields. Currently, irrigation depends on surface water from the El Nubaria Canal, groundwater abstraction, or conjunctive use of both sources. Such extensive reclamation and agricultural expansion have increased the dependence on both Nile water and groundwater resources (Abdel Dayem 1976; Abdel Baki 1983; Embaby 2003) Understanding the geomorphology and land-use evolution of this area is therefore essential for evaluating aquifer systems, groundwater flow, and the vulnerability of groundwater to salinization and seawater intrusion.

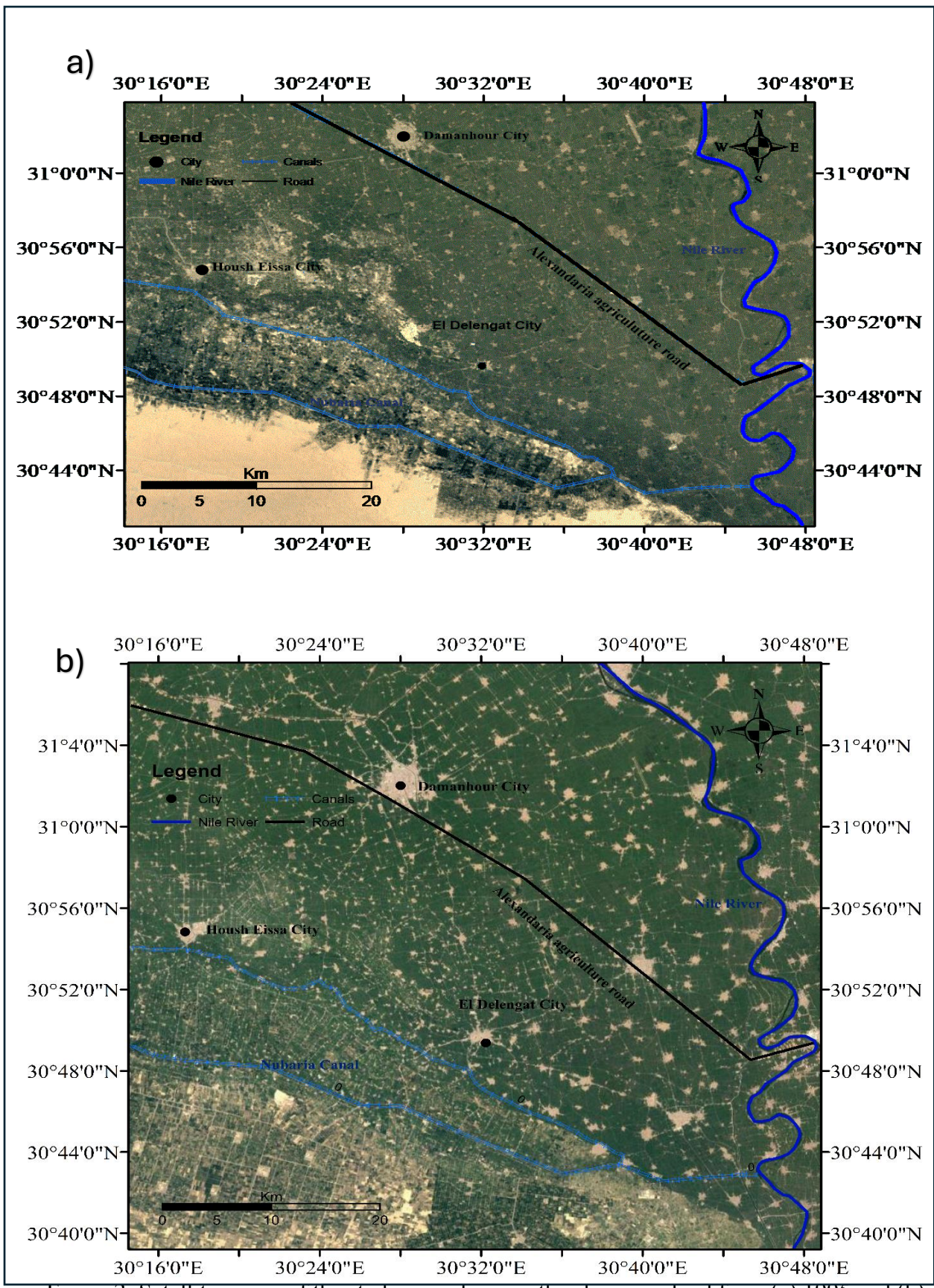


Figure 2: Satellite image of the study area showing the change in land from (a) 1995 and (b) 2023 (adapted from Google Earth Pro, 2025).

### 2.2 Surface and Subsurface Geology

Geologically, the study area comprises a sequence of sedimentary formations extending from the Pliocene to Recent deposits (Figure 3), as documented by (Sandford and Arkell 1939; Said 1962b; El Fayoumy 1964; Omara and Sanad 1975; Shata et al. 1978; El Ghazawi 1982; Abdel Baki 1983; Abdel Wahab 1999). Stabilized dunes and sand sheets dominate the southern part of the area, whereas the central part is covered by wadi deposits composed mainly of sand and gravel, particularly along the El Nubaria Canal. In contrast, the northern part is overlain by Neo-Nile silts and clays, providing fertile soils that sustain intensive agricultural activities. Stratigraphically, the Pleistocene El Nubaria Formation represents the principal water-bearing unit and is subdivided into two members: the Haush Eissa Member, consisting of clay, sand, and sporadic limestone beds (4–65 m thick), and the Alam El Marqab Member, composed of quartz sands and gravels with intercalated clay layers (40–100 m thick), which forms the main aquifer of the region. Beneath these units, the Pliocene deposits, exposed in Wadi El Natrun, consist of clays, sands, and sandy limestones that form the basal aquifer system. The Recent deposits include Nile-derived silts and clays, aeolian sands reaching up to 10 m in thickness, and lagoonal evaporitic facies.

#### 2.3 Tectonics and Structure

The study area, situated in the western Nile Delta, lies within the Marmarican Homocline, a major structural unit of the northern Western Desert. This homoclinal structure represents a transitional zone between the stable Saharan Platform to the south and the tectonically active Mediterranean margin to the north. Within the homocline, the sedimentary succession dips gently northward and northeastward, reflecting the long-term influence of regional subsidence and differential block movements (Shata et al. 1970). The tectonic history of this part of Egypt is marked by successive phases of Mesozoic rifting, Late Cretaceous—Eocene Syrian Arc compression, and Neogene, Quaternary extensional tectonics, which collectively shaped the present structural configuration of the Nile Delta (Kellner et al. 2018; Abd El-Fattah et al. 2021; Shalaby and Sarhan 2023).

The structural setting of the study area itself is characterized primarily by minor faults that produce local variations in the thickness of the Pleistocene aquifer. These faults juxtapose permeable sands against less permeable deposits, thereby exerting control on groundwater flow and storage. Although less pronounced than the major regional elements described elsewhere in the western Nile Delta (El Shazly et al. 1975; Abdel Wahab 1999). The local fault systems play a decisive role in shaping aquifer geometry and promoting secondary salinization. At the surface, Quaternary sediments appear largely undeformed; however, subsurface and geophysical investigations indicate that faulting continues to influence stratigraphic configuration and groundwater dynamics (Saleh 2012; Zaghloul 2013; Abdalsalam et al. 2025).

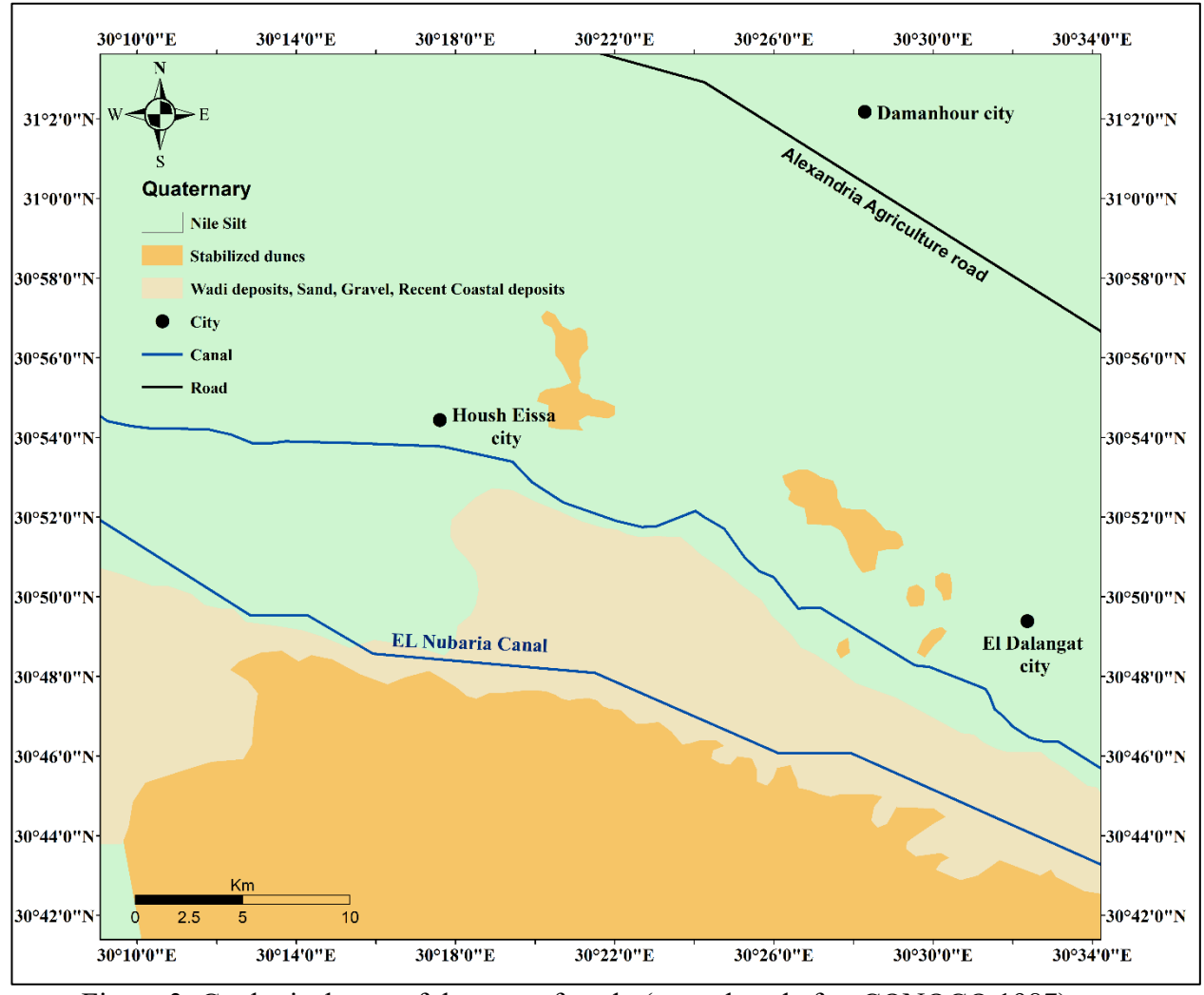


Figure 3: Geological map of the area of study (reproduced after CONOCO 1987).

### 2.4 Hydrogeological Conditions

Groundwater resources in the western Nile Delta are hosted within four principal aquifers: Quaternary (Holocene-Pleistocene), Pliocene, Miocene, and Oligocene formations (Hefny et al. 1991; Sallouma and Gomaa 1997; Embaby 2003a; Khalil et al. 2014; El Osta et al. 2021; Elbeih et al. 2025; Khalifa and Gemail 2025). These aquifers differ in lithology, hydrological characteristics, and spatial distribution. The Pleistocene aquifer consists of sand, gravel, and intercalated clay lenses and occurs under both unconfined and semi-confined conditions (Figure 4). The unconfined part extends across the northern and central sectors, where groundwater levels are shallow and directly influenced by irrigation practices. Semiconfined conditions prevail near the El Nubaria Canal, where clay interbeds reduce vertical permeability. Groundwater depth varies considerably, ranging from a few meters near the northern Delta margin to more than 60 m along the Cairo-Alexandria Desert Road (Abdel Baki 1983). Recharge occurs through subsurface inflow from the Nile Delta aquifer system and infiltration of excess irrigation water (Awad et al. 1997; Abdel Wahab 1999). Historically, the El Nubaria Canal contributed to the aquifer, but as a result of intensive pumping and drainage development, it now acts as a hydraulic sink (Institute 1974). The Holocene deposits, confined to the northern part of the Delta, are composed mainly of Nile-derived silts and clays. Although these fine-grained sediments do not constitute a productive aquifer, they influence near-surface soil moisture conditions and contribute to salinization processes through evapotranspiration. The Pliocene aquifer, exposed mainly in Wadi El Natrun and in the southwestern fringes of the map (Figure 4), consists predominantly of clay with sandy interbeds. It is subdivided into semiconfined and confined layers and is separated from the overlying Pleistocene aquifer by lower Pliocene clays (Othman et al. 2019; Ibraheem et al. 2022). Recharge occurs from the southern Nile Delta via Wadi El-Farigh and from the southwestern part of Wadi El Natrun (Fattah 2017) The underlying Miocene aquifer (Moghra Formation), exposed in Wadi El-Farigh, is composed of coarse sand and sandy clays. It contains a mixture of fossil and renewable water resources (Sharaky et al. 2021) and is underlain by Oligocene deposits, consisting of sandstone, gravel, and basalt sheets that crop out at the southwestern Delta margin (Khaled et al. 2017)

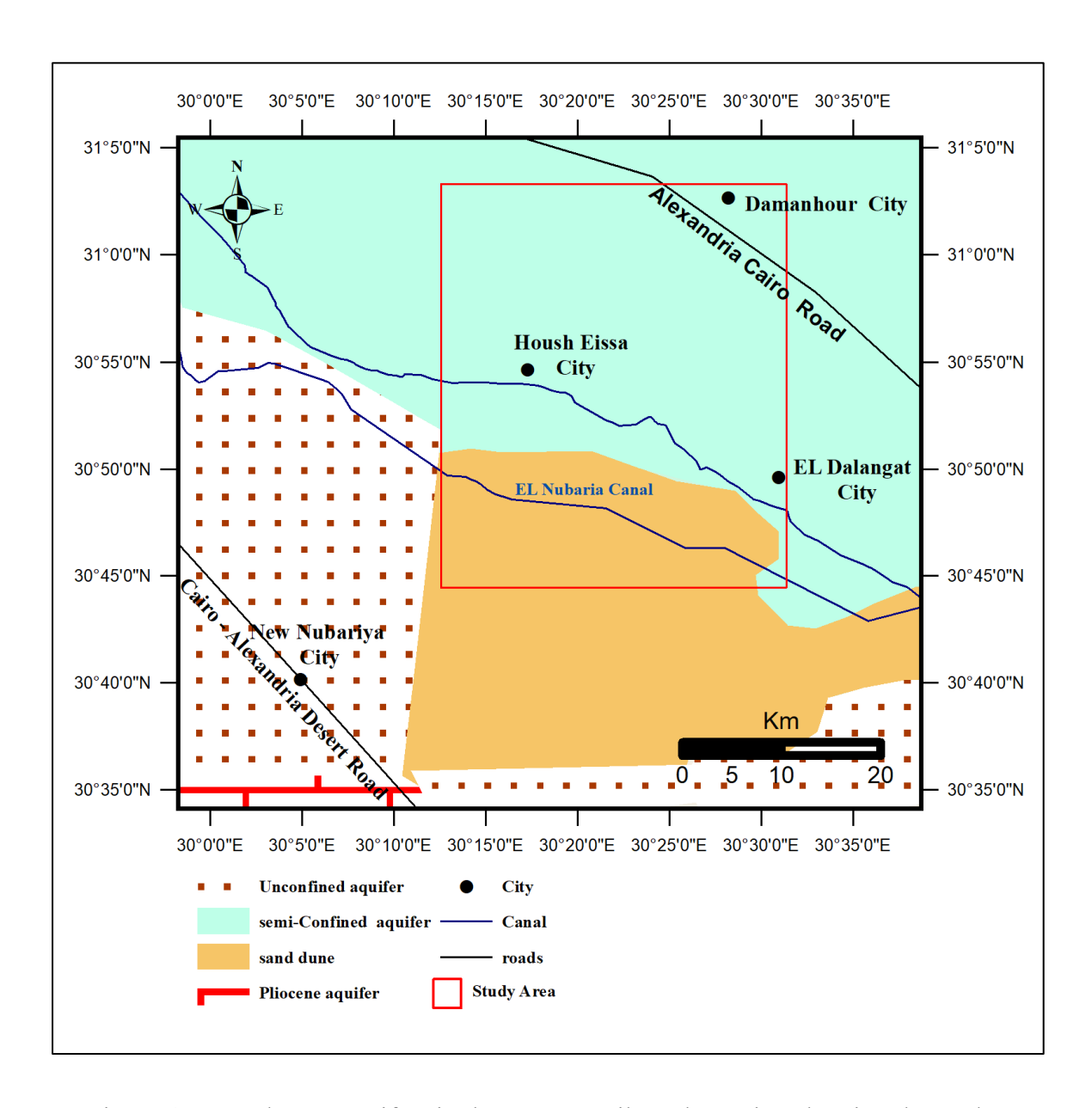


Figure 4: groundwater aquifers in the western Nile Delta region showing the study area (modified after (Zaghloul et al. 2020).

#### 3. Methods

#### 3.1. TDEM Data Acquisition

TDEM method is based on solving Maxwell's equations in their time-dependent form to simulate the transient behavior of electromagnetic fields induced by a pulsed current source (Ward and Hohmann 1988; Zhdanov and Portniaguine 1997). The technique interprets the temporal decay of induced currents and magnetic fields to reconstruct the subsurface distribution of electrical conductivity and stratigraphic layering (Nabighian and Macnae 1991). Unlike frequency-domain methods that assume a steady-state sinusoidal excitation, TDEM captures the transient electromagnetic response, making it particularly effective for detecting time-dependent variations in subsurface conductivity (Constable et al. 1987; Zhdanov 2009).

Operationally, a transmitter loop placed on the surface carries a steady current to establish a primary magnetic field. When this current is abruptly interrupted, the rapid collapse of the primary field induces eddy currents in the underlying conductive medium (Machado 2024). These induced currents generate a secondary magnetic field, the temporal decay of which is governed by the electrical conductivity of subsurface materials (Spies and Frischknecht 1991). A receiver coil positioned at the surface records the transient voltage response arising from the time-varying secondary magnetic flux. According to Faraday's law of induction, the rate of voltage decay reflects the rate of eddy-current dissipation, with deeper currents decaying more slowly. The resulting temporal decay curve thus provides depth-dependent information on subsurface resistivity (Nabighian and Macnae 1988).

The apparent resistivity  $\rho_a(t)$ , as a function of measurable voltage decay e(t) and time t, is computed following (Keller and Kaufman 1983):

$$\rho_a(t) = \frac{k_2 M^{2/3}}{[e(t)]^{2/3} [t]^{5/3}} \tag{1}$$

where  $\rho_a(t)$  is the apparent resistivity at time t ( $\Omega \cdot m$ ), e(t) is the voltage decay (V), t is the time after the transmitter current is turned off (s),  $k_2$  is a constant, and M is the transmitter moment, defined as the product of the transmitter current I (A) and the loop area A ( $m^2$ ).

A total of 25 TDEM soundings were acquired across the study area (Figure 5) using a coincident-loop configuration, in which a single 50 m loop served as both transmitter and

receiver (Fitterman and Stewart 1986). Data were collected using a SIROTEM MK-3 system. Each sounding was recorded at four gain settings (0.1, 1, 10, and 100). The decay curves exhibiting the highest signal-to-noise ratios, characterized by a smooth decline, minimal scatter, and stable late-time behavior, were selected for further processing and interpretation (Hegarty et al. 2016; Xing et al. 2024).

Five profiles were established (A–A', B–B', C–C', D–D', and E–E'), oriented west–east to cover the main hydrogeological features of the area. Profiles A–A', B–B', C–C', D–D', and E–E' comprised soundings 1–5, 6–10, 11–15, 16–20, and 21–25, respectively.

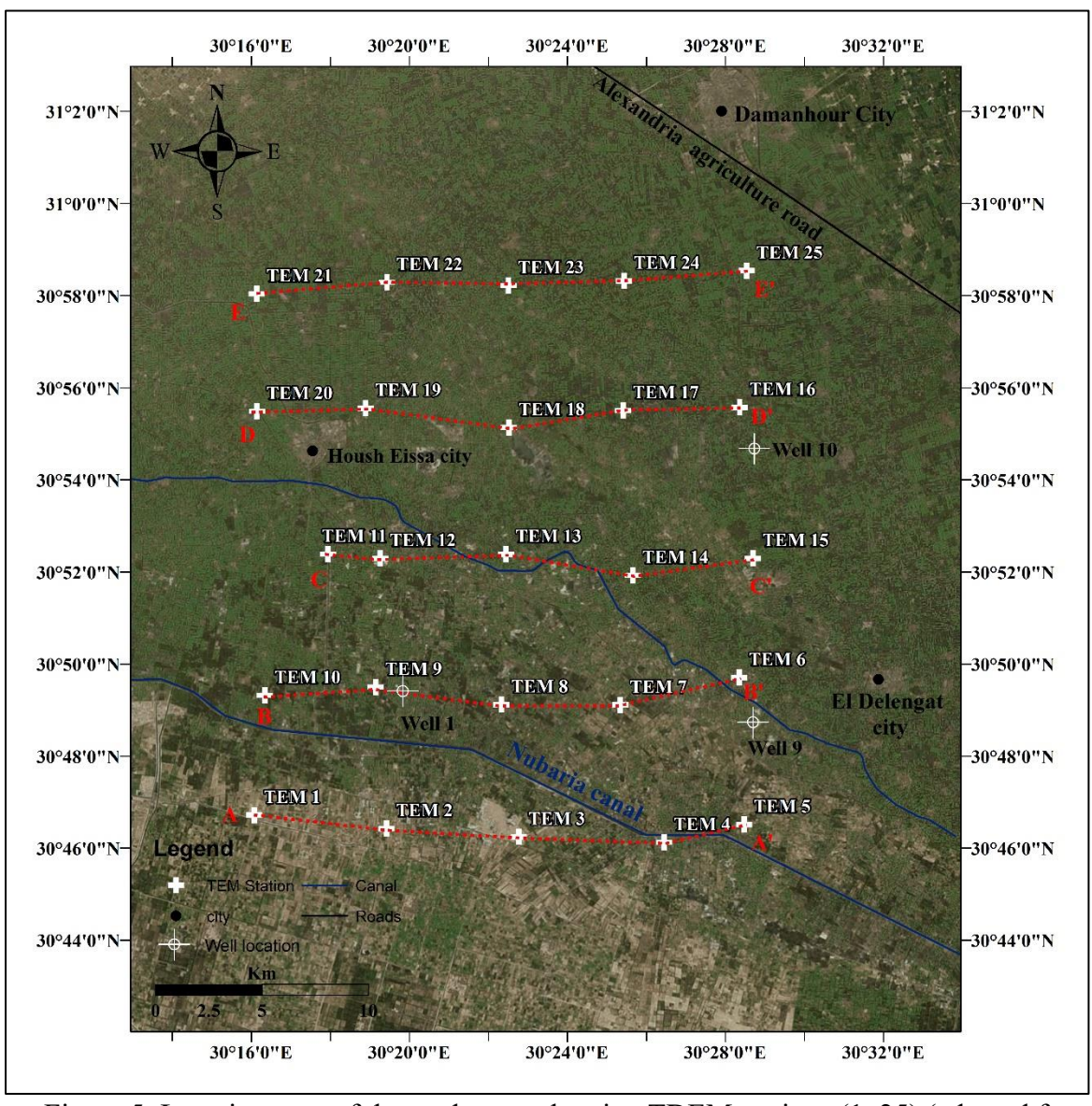


Figure 5: Location map of the study area showing TDEM stations (1–25) (adapted from Google Earth Pro, 2025).

### 3.2. TDEM Inversion and Interpretation

One-dimensional (1D) resistivity inversion was performed using ZondTEM1D software, applying a smooth-model inversion technique to produce continuous resistivity models that resolve gradual subsurface variations (Constable et al. 1987). This approach effectively delineates lithological boundaries, aquifer zones, and fault-related features. During inversion, model parameters were iteratively adjusted to minimize the misfit between measured and calculated decay curves. The model fit was quantified by the Root Mean Square Error (RMSE), where values below 10% indicate an accurate and geophysically consistent representation of the subsurface.

The initial TDEM models were constrained using lithological logs from three boreholes (1, 9, and 10) reported by (Salem and Osman 2016) along with regional aquifer maps, to ensure realistic subsurface layering. Inversion parameters were refined iteratively until the modeled resistivity profiles aligned with the known stratigraphy, and the results were validated against borehole data, confirming a strong correlation between the resistivity-derived layers and the actual lithological units. Figures 6 to 8 illustrate the correspondence between TDEM stations 6, 9, and 16 and boreholes 9, 1, and 10, respectively, where resistivity variations clearly reflect the identified subsurface formations and show the vertical distribution of the electrical properties. The inversion results delineated multiple resistivity layers, with high-resistivity zones representing unsaturated or coarse sandy layers and low-resistivity zones corresponding to clay-rich or water-saturated materials (Archie 1942). Nevertheless, careful interpretation was essential, as clay-rich horizons and saline-saturated sands can exhibit similarly low resistivity values, leading to potential ambiguity in distinguishing between them.

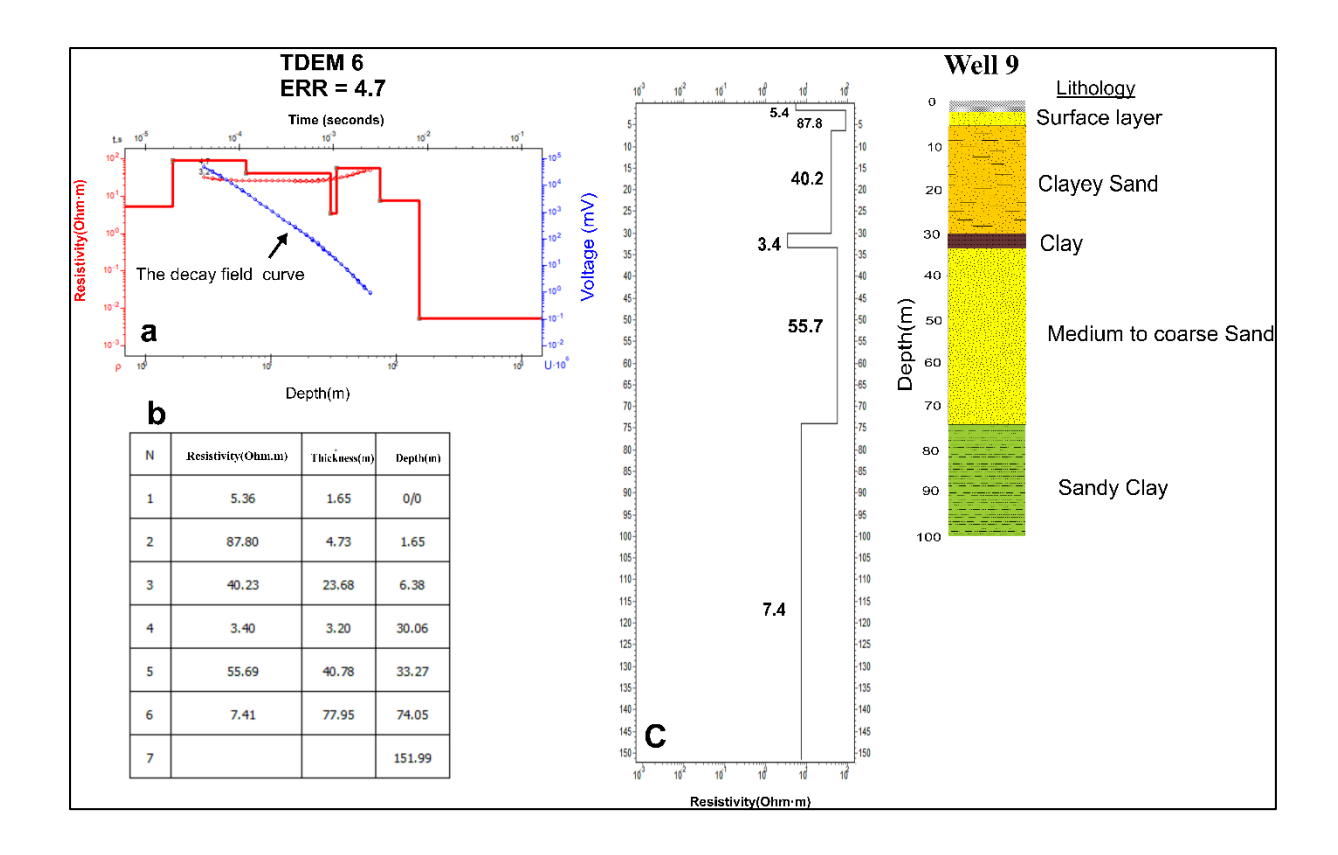


Figure 6. Correlation between geoelectric and borehole data. (a) Decay voltage (blue line) and apparent resistivity (red line) curves over time for TDEM station 6. (b) 1D inverted resistivity-depth profile derived from the TDEM data at station 6 (c) Lithological log from well 9 illustrating alignment with the interpreted geoelectric layers.

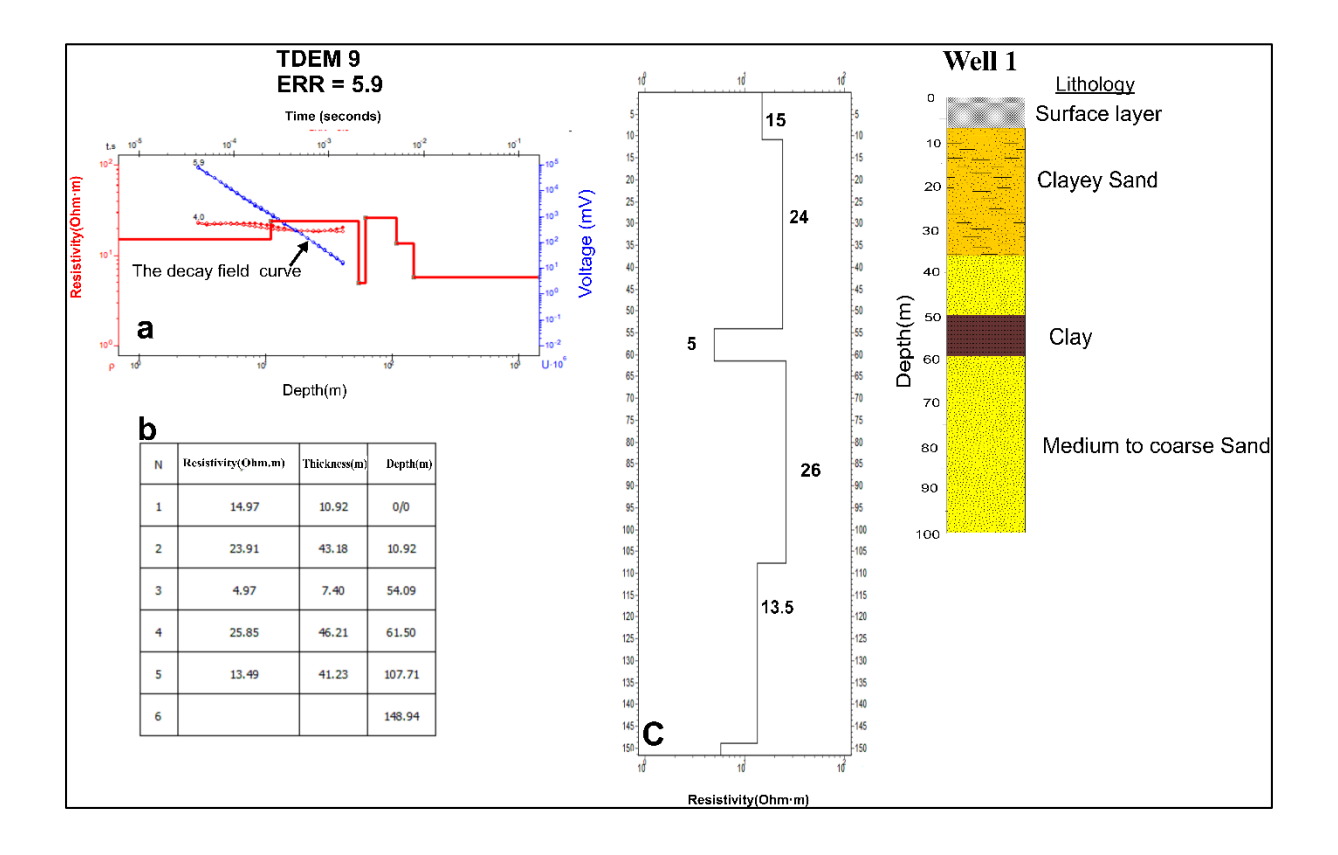


Figure 7. Correlation between geoelectric and borehole data. (a) Decay voltage (blue line) and apparent resistivity (red line) curves over time for TDEM station 9. (b) 1D inverted resistivity-depth profile derived from the TDEM data at station 9 (c) Lithological log from well 1 illustrating alignment with the interpreted geoelectric layers.

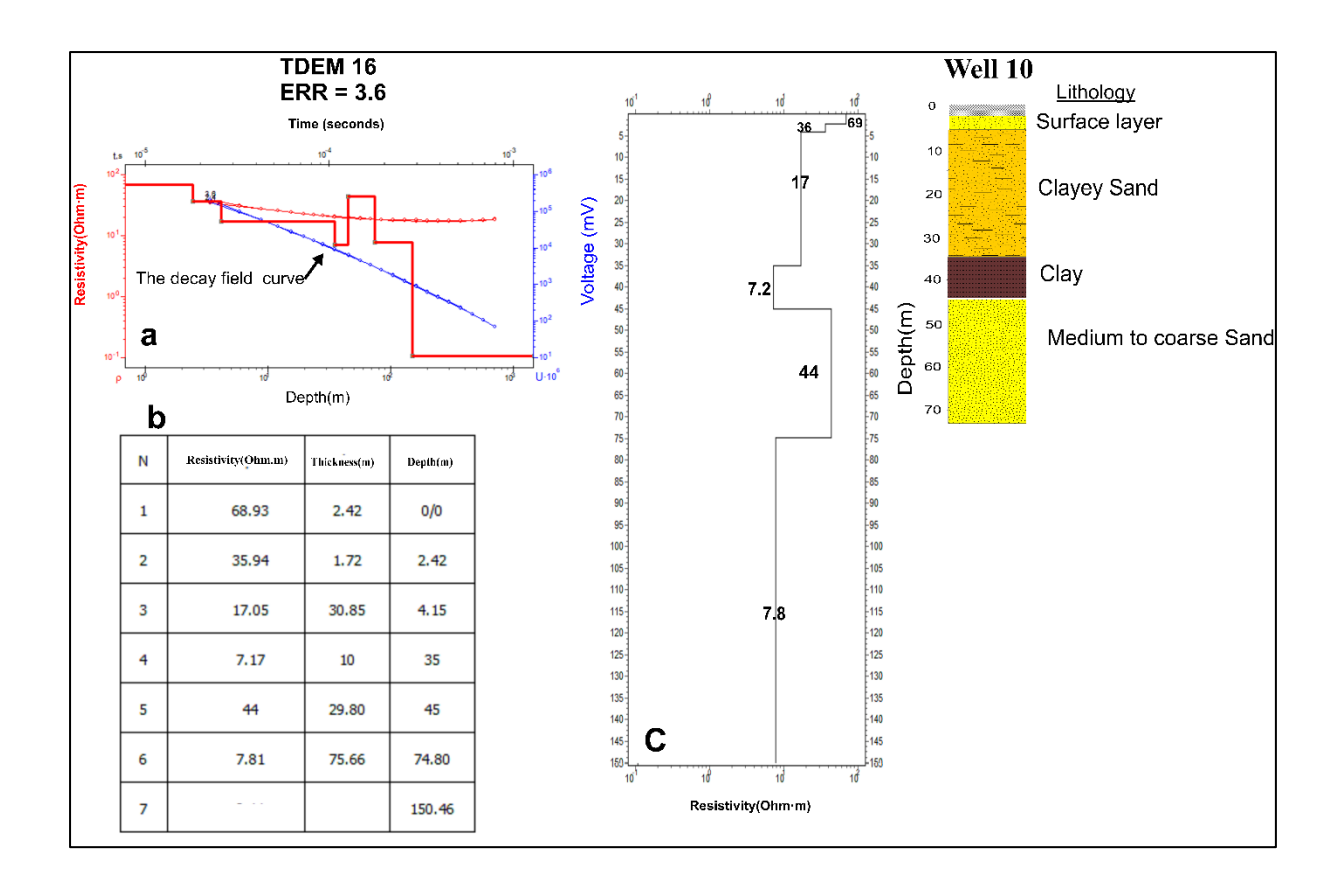


Figure 8. Correlation between geoelectric and borehole data. (a) Decay voltage (blue line) and apparent resistivity (red line) curves over time for TDEM station 16. (b) 1D inverted resistivity-depth profile derived from the TDEM data at station 16 (c) lithological log from well 10 illustrating alignment with the interpreted geoelectric layers.

# 3.3 Hydrochemical Sampling and Laboratory Analyses

A total of 30 water samples, including both groundwater and surface water, were collected from the study area to ensure broad spatial coverage, with sampling depths ranging between 5 m and 167 m. Samples were collected in pre-cleaned polyethylene bottles that were thoroughly rinsed with the respective sample water before collection. All samples were preserved at 4 °C until laboratory analysis. Groundwater samples were obtained from wells distributed across cultivated, residential, and canal zones. The geographic coordinates of all sampling sites were recorded using a Garmin GPSMAP 86sci device.

Field measurements of pH and electrical conductivity (EC) were performed in situ using a YSI Model 63 multiparameter instrument. Total dissolved solids (TDS) were estimated by EC measurements using a locally derived conversion factor (k = 0.64), according to the relation:

TDS (mg/L) = 
$$k \times EC$$
 ( $\mu S/cm$ ) (2)

Each well was hand-pumped for approximately 10–15 minutes before sampling to ensure the stabilization of field parameters. Total hardness (TH) was determined using the classical relation proposed by Sawyer et al. (1967):

TH (as CaCO<sub>3</sub>, mg/L) = 
$$(Ca^{2+} + Mg^{2+})_{meq/L} \times 50$$
 (3)

Major cations (Ca<sup>2+</sup>, Mg<sup>2+</sup>, Na<sup>+</sup>, K<sup>+</sup>) and anions (Cl<sup>-</sup>, SO<sub>4</sub><sup>2-</sup>, HCO<sub>3</sub><sup>-</sup>, NO<sub>3</sub><sup>-</sup>) were analyzed following the standard procedures of the American Public Health Association (APHA) 2017). Calcium and magnesium were determined by EDTA titration, sodium and potassium by flame photometry, chloride by argentometric titration, sulfate by the turbidimetric method, and bicarbonate by acid–base titration. Nitrate was measured spectrophotometrically. The ironic-balance error (IBE) was maintained within  $\pm$  5% to ensure analytical accuracy, calculated as:

IBE (%) = 
$$\frac{\Sigma \text{Cations} - \Sigma \text{Anions}}{\Sigma \text{Cations} + \Sigma \text{Anions}} \times 100$$
 (4)

Hydrochemical facies were classified using the Piper diagram (Piper 1944), while Gibbs diagrams (Gibbs 1970) were applied to identify the dominant geochemical processes influencing groundwater chemistry. To evaluate groundwater suitability for drinking and

irrigation, several indices were calculated, including the Water Quality Index (WQI), Sodium Adsorption Ratio (SAR), Sodium Percentage (Na%), and Magnesium Hazard (MH). These were determined as follows (all ionic concentrations expressed in meq/L):

$$SAR = \frac{Na^{+}}{\sqrt{(Ca^{2+} + Mg^{2+})/2}}$$
 (5)

$$Na\% = \frac{(Na^{+}+K^{+})\times 100}{Ca^{2^{+}}+Mg^{2^{+}}+Na^{+}+K^{+}}$$
 (6)

$$MH = \frac{Mg^{2+} \times 100}{Ca^{2+} + Mg^{2+}}$$
 (7)

SAR reflects the potential of sodium to replace calcium and magnesium in soil exchange sites, affecting soil permeability and structure. Na% indicates the relative sodium hazard in irrigation water, while MH > 50 % suggests excessive magnesium that may impair soil quality (Joshi et al. 2009; Shankar et al. 2018).

Spatial distribution maps of TDS, major ions, WQI, SAR, Na%, and MH were generated using Python-based GIS interpolation to visualize hydrochemical variability across the study area and to delineate zones of differing water quality for drinking and agricultural uses.

# 4. Results

# **4.1 TDEM**

Figures 9–13 present cross-sections derived from the interpretation of TDEM curves oriented in the W–E direction. These sections delineate the study area into six distinct geoelectric units, classified according to their resistivity values.

- 1. Weathered Zone (Surface Layer): Extending from the surface to depths of 2–20 m, this heterogeneous layer exhibits resistivity values ranging from 5 to 412  $\Omega$ ·m, reflecting mixed topsoil, sands, silts, clay, and gravel.
- 2. Shallow Aquifer (Clayey Sand layer): Occurring at depths of 10–40 m with resistivity values of 10–25 Ω·m(Figure 14), this aquifer is thickest (20–30 m) in the southern and central profiles (A–A′ to C–C′; Figures 9–11), where it functions as an unconfined aquifer. It thins markedly northward and is almost absent in profiles D–D′ and E–E′ (Figures 12–13).
- 3. Main Aquifer (Medium to Coarse Sand): This principal water-bearing unit occurs at depths of 30–120 m with resistivity values of 25–70 Ω·m and thickness ranging from 36 to 66 m (Figures 19–20). It is well-developed and continuous in the southern and central profiles (A–A′ and B–B′; Figures 9–10) but becomes thinner and discontinuous northward (profiles C–C′ to E–E′; Figures 11–13). Clay intercalations locally interrupt it, as seen in profile A–A′ (Figure 9).
- 4. Confining Clay Layer: This unit shows variable geometry, defined by very low resistivity values (1.3–8 Ω·m). In profile A–A' (Figure 9), it cuts into the main aquifer, reducing connectivity and productivity. In profiles B–B' to D–D' (Figures 10–11), it appears above the main aquifer, acting as a protective aquitard against surface contamination.
- 5. Sandy Clay Layer: With resistivity values of 1.3–14.5 Ω·m, this unit occurs as a thin (10–30 m) discontinuous horizon in the south and center (profiles A–A' to C–C'; Figures 9–11) but thickens substantially in the north (profiles D–D' to F–F'; Figures

- 11−13), extending to ~150 m depth. Here it functions as a semi-confining unit, though its protective role is weakened where truncated by saline water.
- 6. Seawater Intrusion: This highly conductive layer (<1 Ω·m) is absent in the southern profiles (A–A' to C–C'; Figures 9–11) but becomes increasingly prominent northward. It is most extensive in the northern profiles (E–E' and F–F'; Figures 13–16), where it extends from ~70 m to the survey base at 150 m, exceeding 80 m thickness. This defines the lower limit of usable freshwater resources.

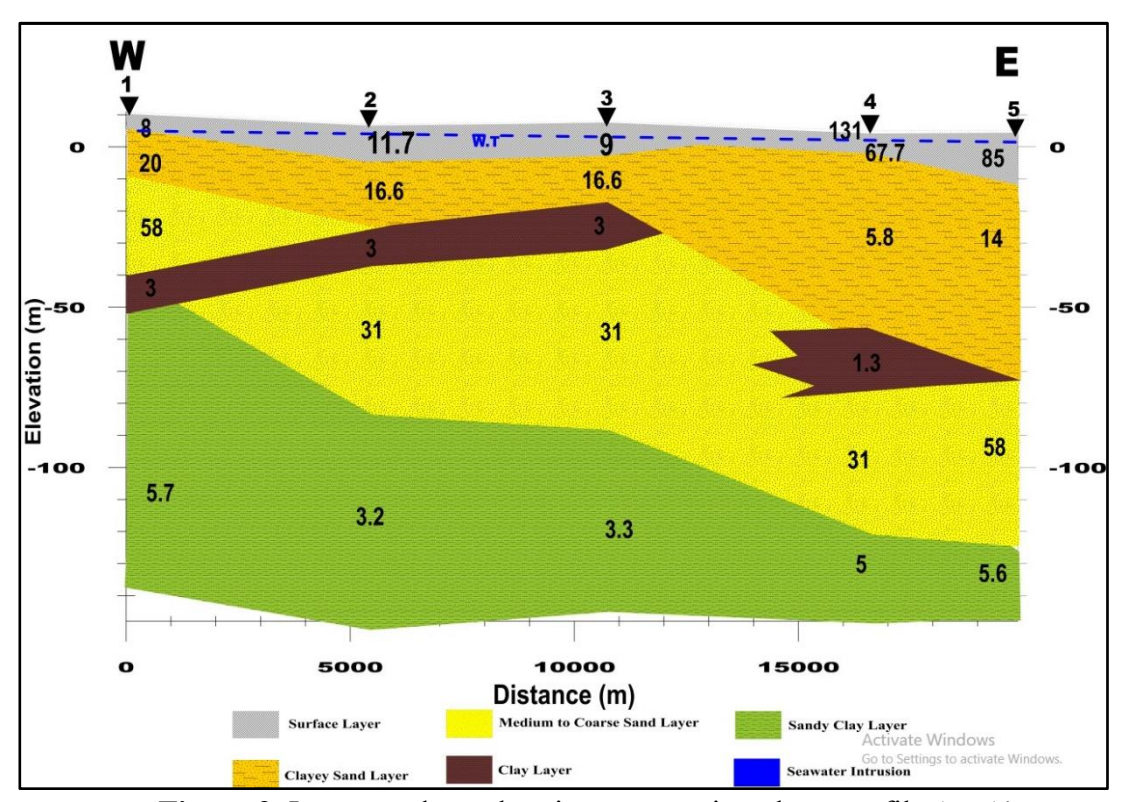


**Figure 9.** Interpreted geoelectric cross-section along profile A - A'.

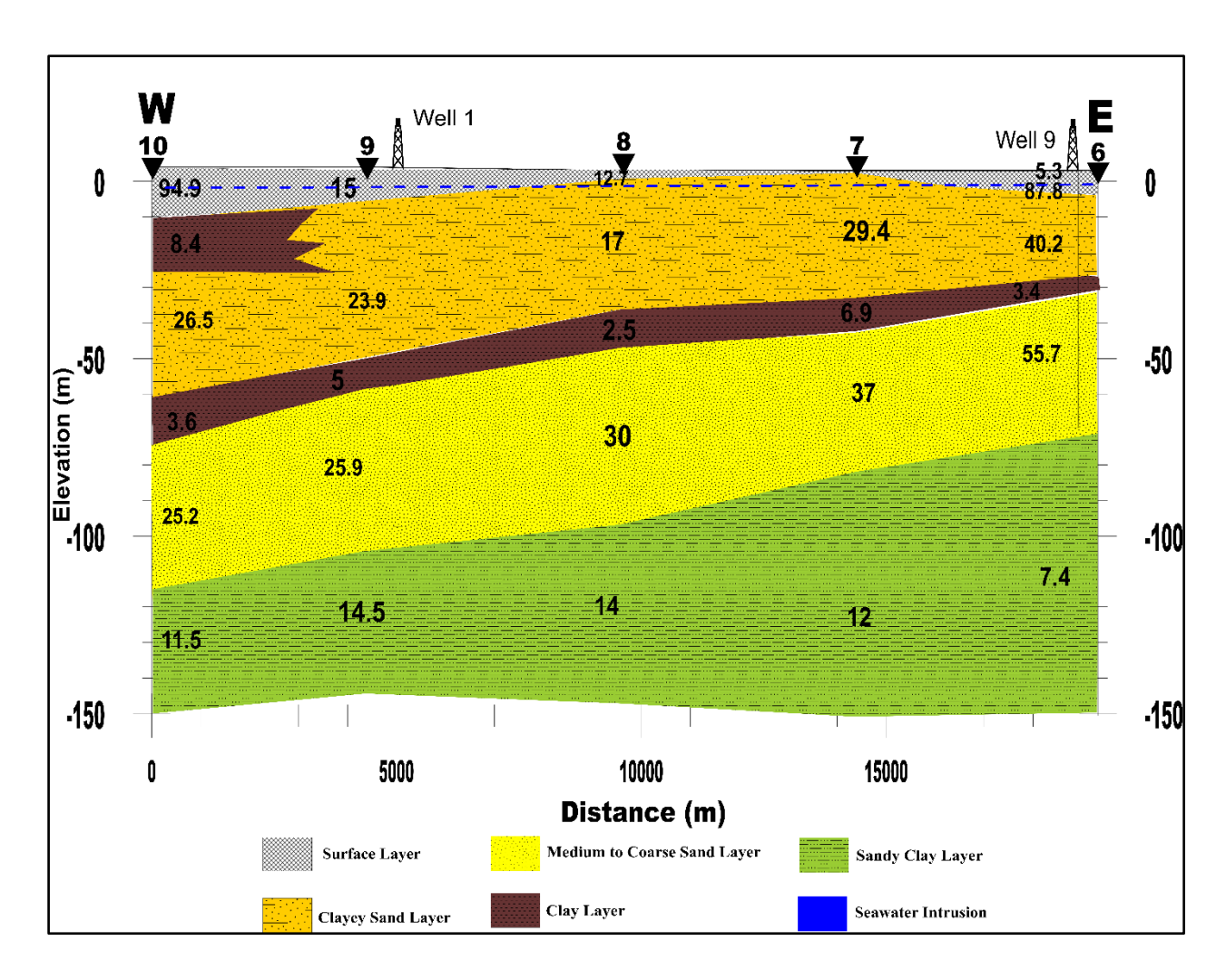


**Figure 10.** Interpreted geoelectric cross-section along profile B - B'.

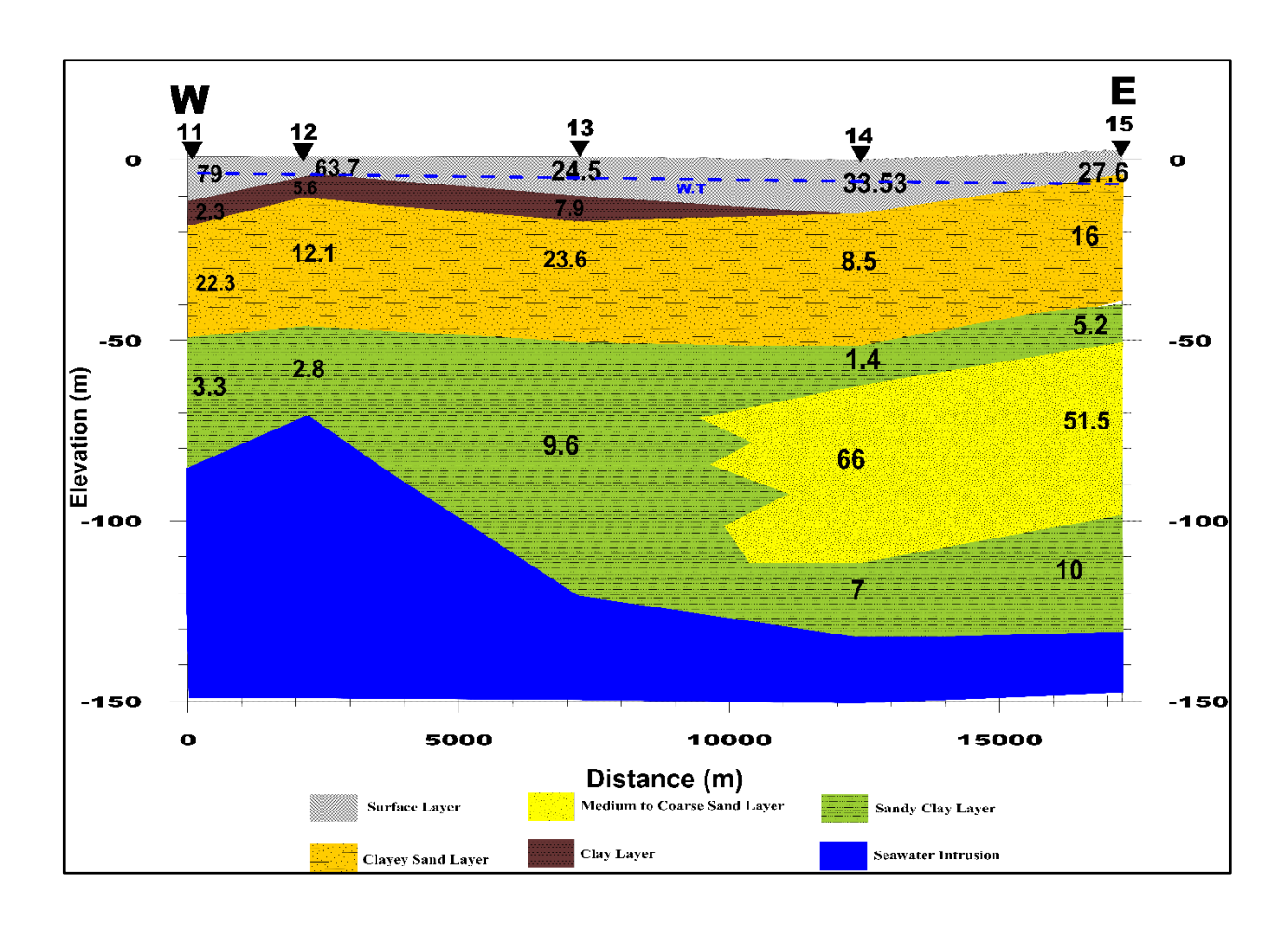


**Figure 11.** Interpreted geoelectric cross-section along profile C – C'.

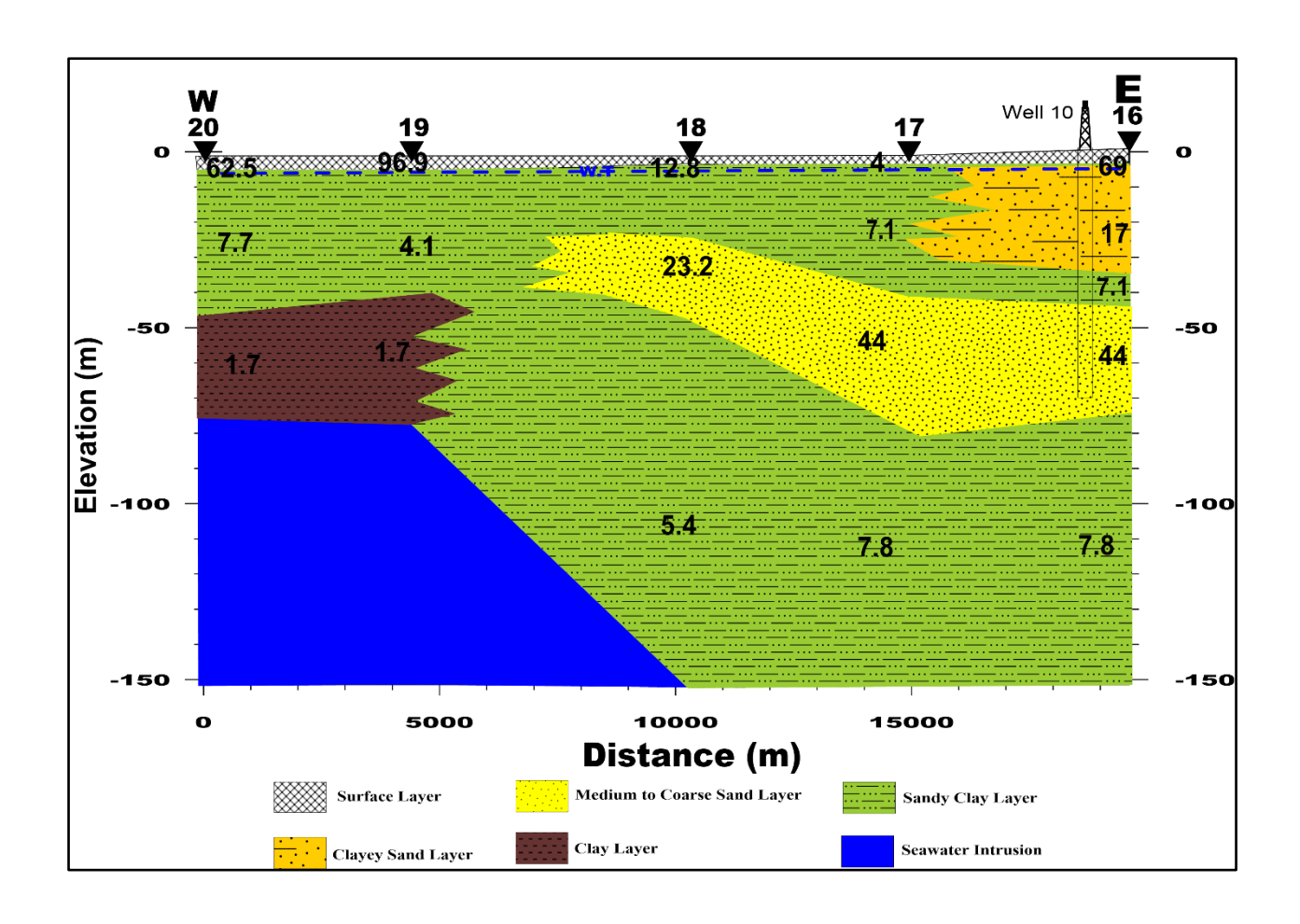
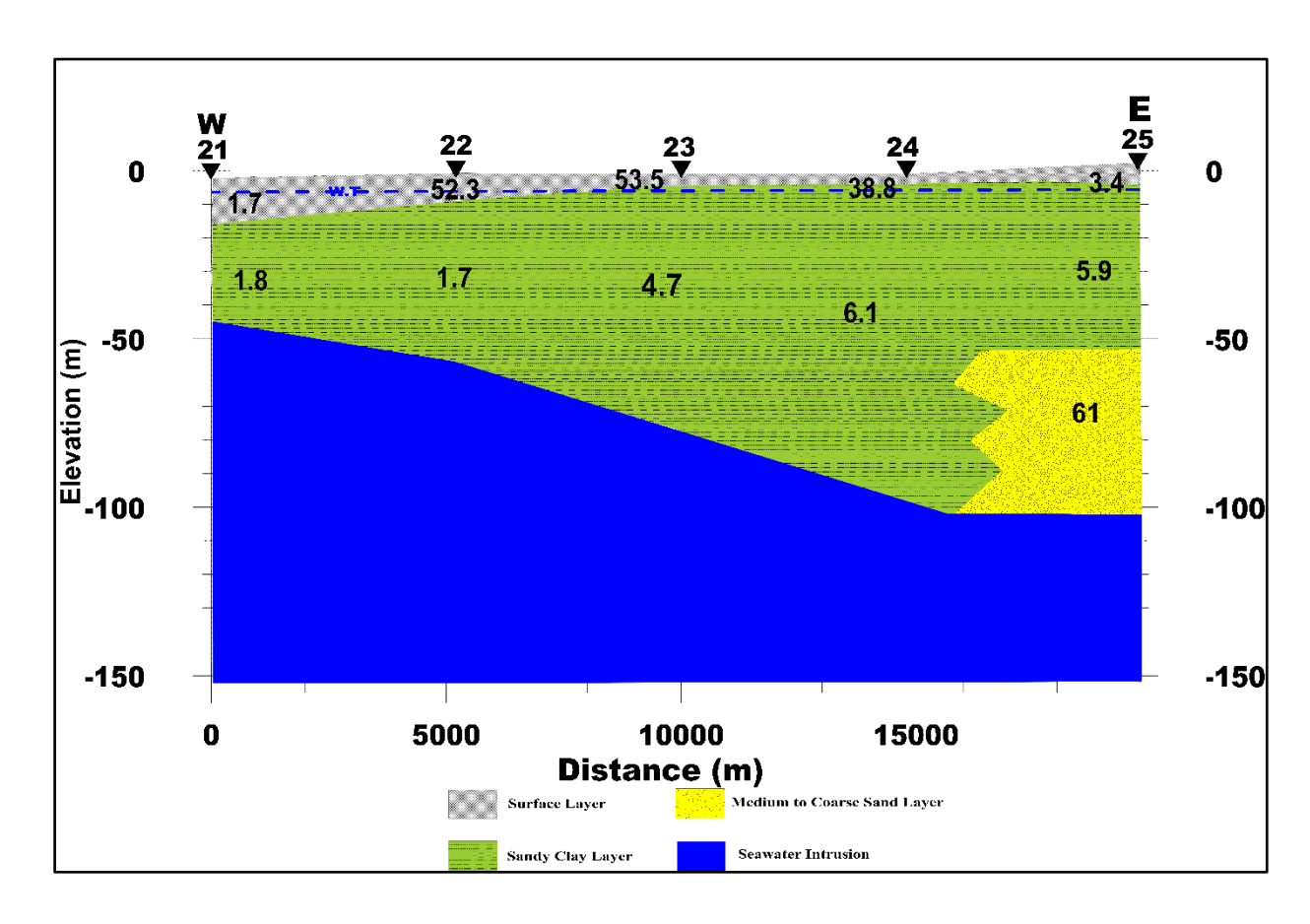


Figure 12. Interpreted geoelectric cross-section along profile D-D'



**Figure 13.** Interpreted geoelectric cross-section along profile E–E'.

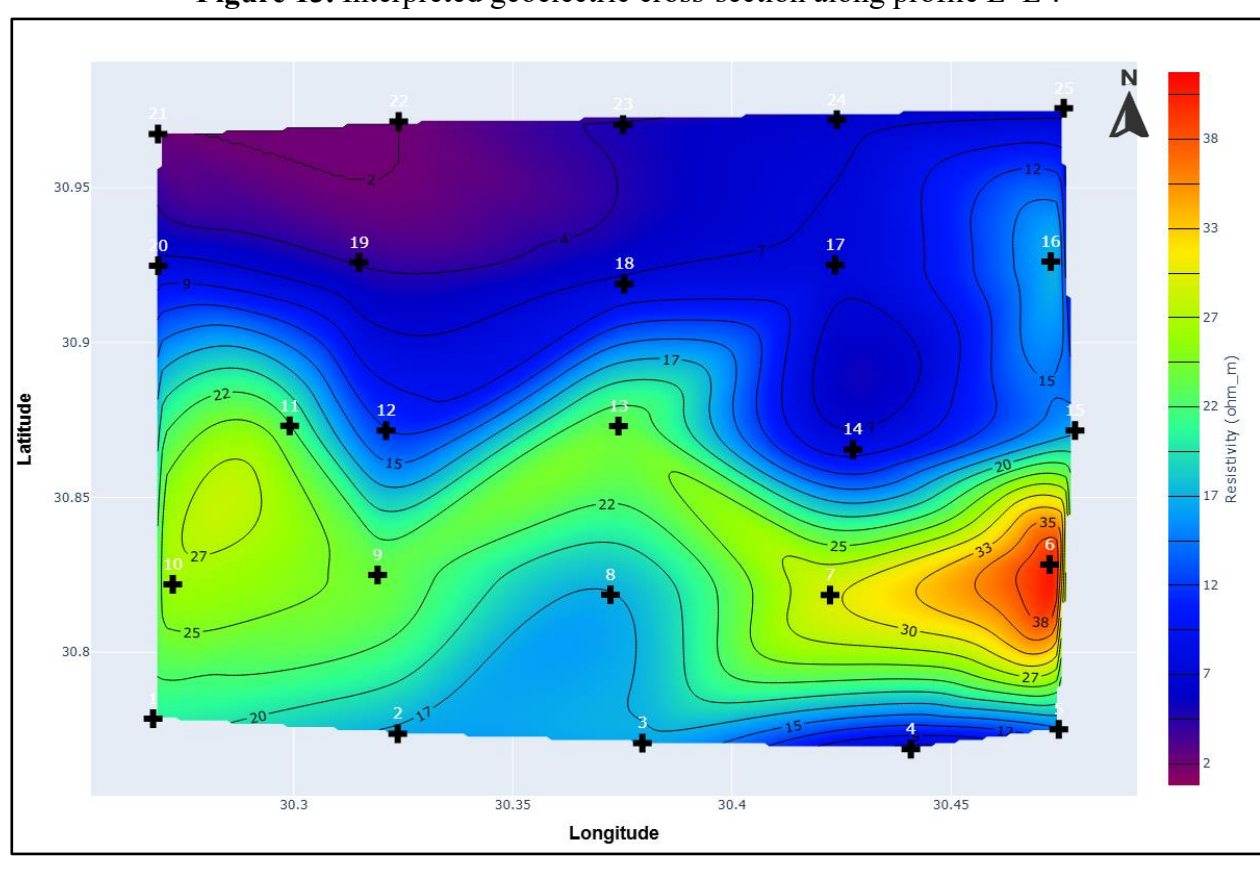


Figure 14. True electrical resistivity map of the shallow aquifer in the study area.

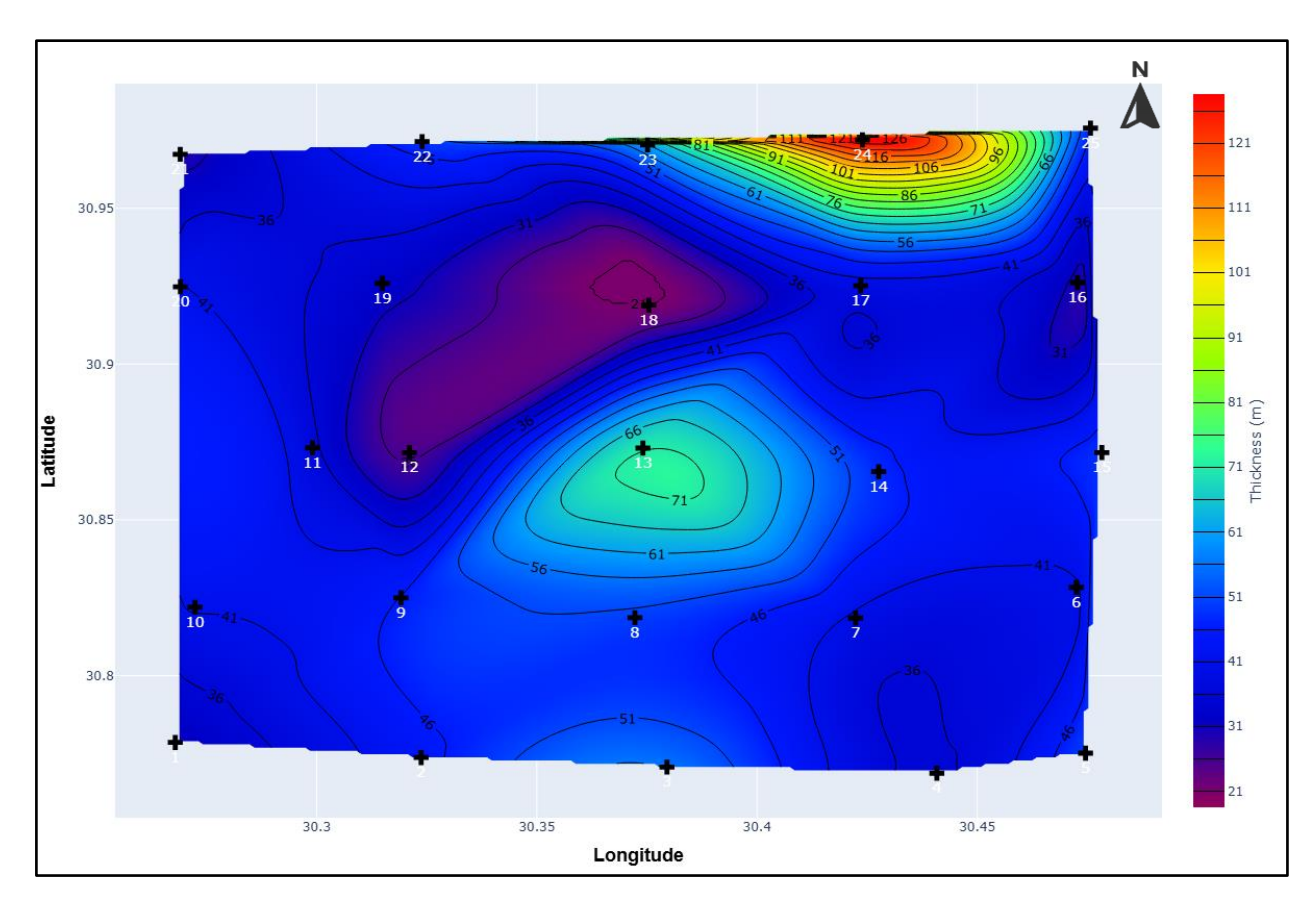


Figure 15. Thickness map of the main aquifer in the study area.

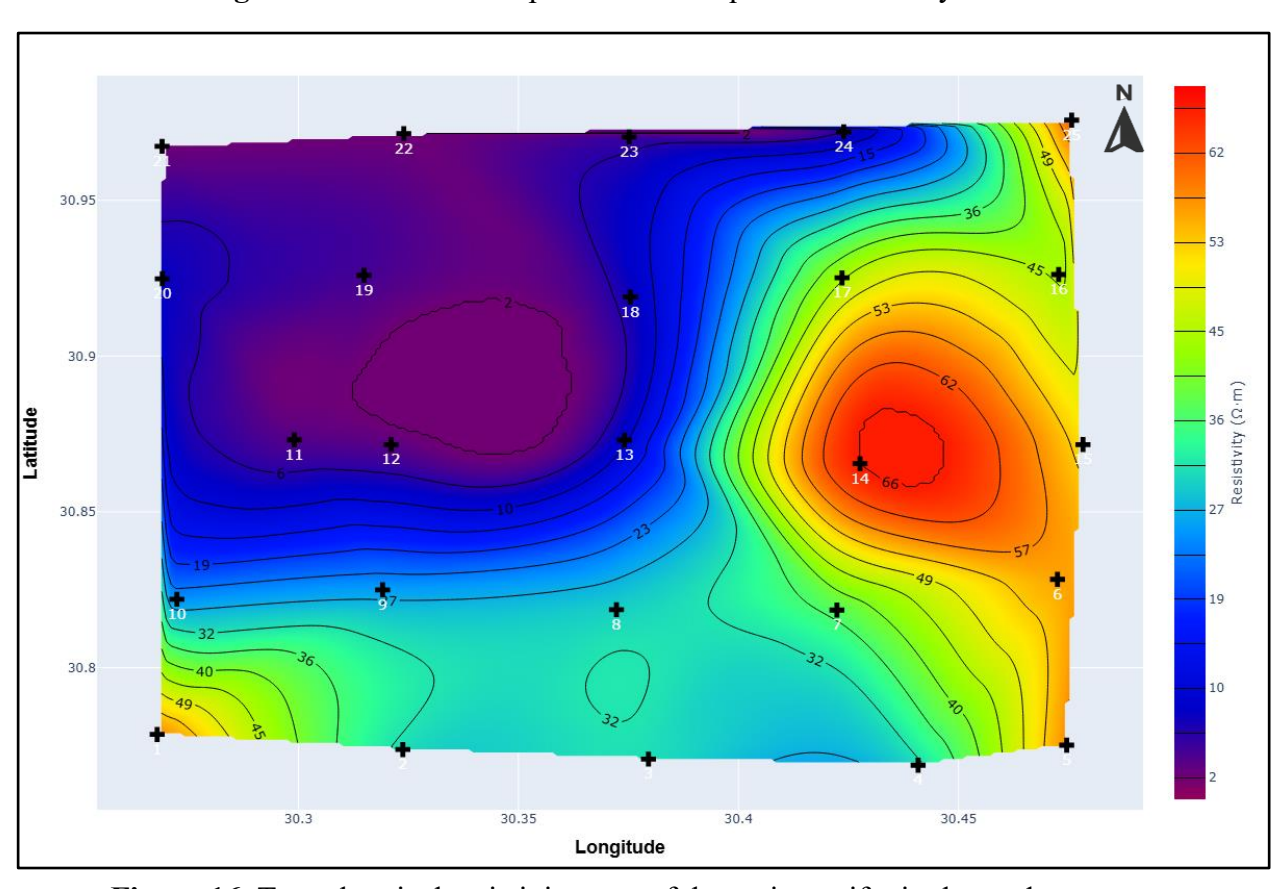
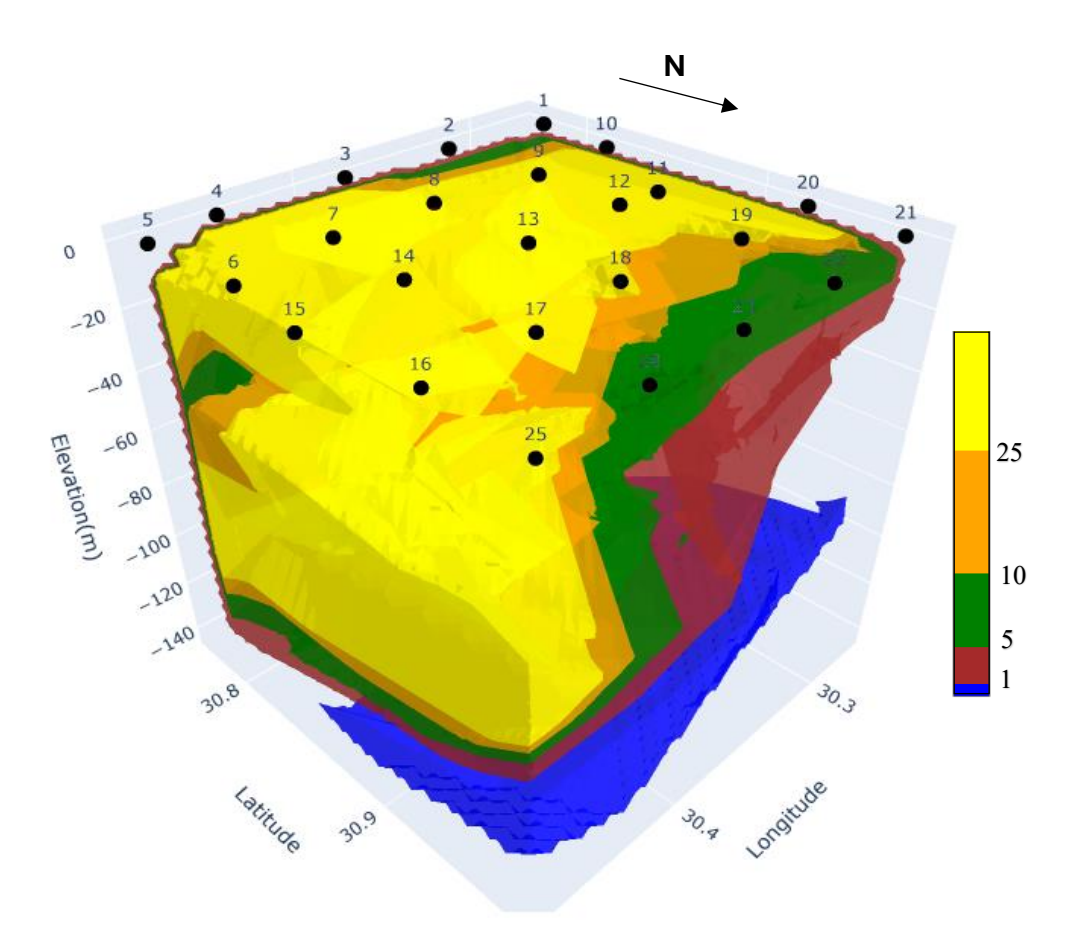


Figure 16. True electrical resistivity map of the main aquifer in the study area.

Figure 17 shows the 3D distribution of interpolated resistivity values from the inversion results of all 25 TEM soundings. The colors in the model represent discrete resistivity intervals rather than lithology itself; however, when integrated with 1D interpretations and geological context, they can be linked to key hydrogeological units. In general, resistivities exceeding 25  $\Omega$ ·m correspond to the main freshwater aquifer, whereas values below 1  $\Omega$ ·m delineate the saline intrusion plume. Intermediate resistivities (1–25  $\Omega$ ·m) occur in layered sequences, with shallow weathered and sandy horizons at the higher end, and clay to sandy-clay horizons at the lower end.

The 3D model highlights both the geometry and extent of the main freshwater aquifer. The high-resistivity body (>25  $\Omega$ ·m), representing medium-to-coarse sand, is thick and laterally continuous in the southern and central sectors, confirming the presence of a well-developed aquifer with significant groundwater potential. In contrast, the northern part of the model reveals a marked thinning of the aquifer due to the encroachment of a deep conductive body (<1  $\Omega$ ·m), corresponding to seawater intrusion. This saline plume ascends toward the surface, progressively reducing freshwater volume and accounting for the sharp north-south contrast in groundwater quality and productivity. This contrast is clearly expressed in the resistivity data, with higher values (>25  $\Omega$ ·m) in the north indicating freshwater-bearing aquifers, and lower values (<5  $\Omega$ ·m) in the south marking saline or clay-rich zones. Interbedded sandy-clay and clay horizons act as semi-confining layers that subdivide the aquifer into compartments with distinct hydraulic properties. These layers also redirect and concentrate saline movement, creating preferential pathways for intrusion rather than allowing a uniform flow.



**Figure 17.** 3D distribution of interpolated resistivity values from the inversion results of all 25 TEM soundings.

### 3.2 Hydrochemical Characteristics

## 3.2.1 Statistical Summary

The hydrochemical composition of groundwater samples from both the shallow and main aquifer indicates marked variability, reflecting differences in recharge processes, lithological controls, and anthropogenic pressures. A descriptive statistical summary of the analyzed parameters is presented in Table 1, along with the World Health Organization ((WHO) 2011) standards for comparison. The WHO (2011) does not provide specific health-based guideline limits for calcium, magnesium, or sulfate in drinking water. Calcium and magnesium are essential minerals, typically ranging from 10–100 mg/L and 5–50 mg/L, respectively, while sulfate concentrations in natural groundwater generally range from 2 to 80 mg/L but may locally exceed 250 mg/L due to the dissolution of gypsum or anhydrite (Freeze and Cherry 1979; Hem 1985)

Parameter	Unit	Shallow Aquifer (n=17)				Main Aquifer (n=12)				WIIO (2011)
		Min	Max	Mean	Std. Dev.	Min	Max	Mean	Std. Dev.	WHO (2011)
TDS	mg/L	388	9610	2468	2448	553	9150	2147	2753	500
$Ca^{2+}$		0	600	96.7	156.1	1.23	330	92.9	104.8	100*
$Mg^{2+}$		6.99	976	125.9	204.7	6.99	612.4	104.9	159.2	50*
$Na^+$		50	1076.9	349.0	277.9	80.9	1258.5	332.1	327.1	200
Cl-		20	3900	497.0	876.0	20	3000.2	491.4	851.8	250
$\mathrm{SO}_4{}^{2-}$		15	750.7	242.4	225.4	47	1000	327.6	295.8	250*
$\mathrm{NO_{3}^{-}}$		0.19	948	154.6	282.6	0.19	245	247.8	698.6	50

Table 1. Statistical summary of physicochemical parameters in shallow and main aquifers compared with ((WHO) 2011) standards.

# 3.2.2 Spatial distribution maps of TDS

The spatial distribution of Total Dissolved Solids (TDS) in the shallow aquifer (Figure 18 ranges from 388 to 9,610 mg/L, showing a clear spatial variation across the study area. The central zone, where TDS values range from 388 to 2,232 mg/L, represents the freshest groundwater and indicates the influence of active recharge and dilution by relatively unmineralized water. Moving outward from the center, TDS gradually increases to 3,000–6,000 mg/L, marking transitional or mixing zones affected by irrigation return flow, partial saline seepage, and agricultural inputs. Within these zones, nitrate (NO<sub>3</sub><sup>-</sup>) concentrations are notably

high, reaching 914 mg/L at Well 2 and 753 mg/L at Well 3, reflecting fertilizer leaching and wastewater infiltration associated with intensive agricultural activity. The highest TDS values (6,800–9,610 mg/L) occur along the northeastern and southern boundaries, where the aquifer is influenced by the presence of clay layers, seawater intrusion, evaporation, and agricultural salinization. These marginal zones also correspond to high chloride (Cl<sup>-</sup>) concentrations, confirming that chloride governs the natural salinity gradient in the shallow aquifer. Although the central zone remains comparatively fresh, several wells still exceed the WHO (2011) drinking-water limit of 500 mg/L, indicating moderate mineralization even within the recharge area.

In the main aquifer (Figure 19), TDS values range from 553 to 9,150 mg/L (mean  $\approx$  2,147 mg/L), displaying a more complex spatial pattern. The northern and eastern sectors record the highest salinity levels (>9,000 mg/L), confirming the upward movement of deep saline water into the aquifer. These zones are also characterized by elevated chloride concentrations (up to 3,000.2 mg/L), indicating the dominant role of marine and evaporitic sources in groundwater mineralization. The central region exhibits moderate TDS (533–1,500 mg/L) but locally elevated nitrate (up to 245 mg/L at Well 5), suggesting leakage through semi-confining layers and structural discontinuities that allow vertical infiltration of surface contaminants. Toward the south, TDS decreases locally to about 533-1400 mg/L at Well 2 and 12, reflecting the influence of fresh recharge and high-permeability sand layers, while localized increases in sulfate (up to 1,000 mg/L) and chloride indicate the early stages of mineralization and seawater encroachment.

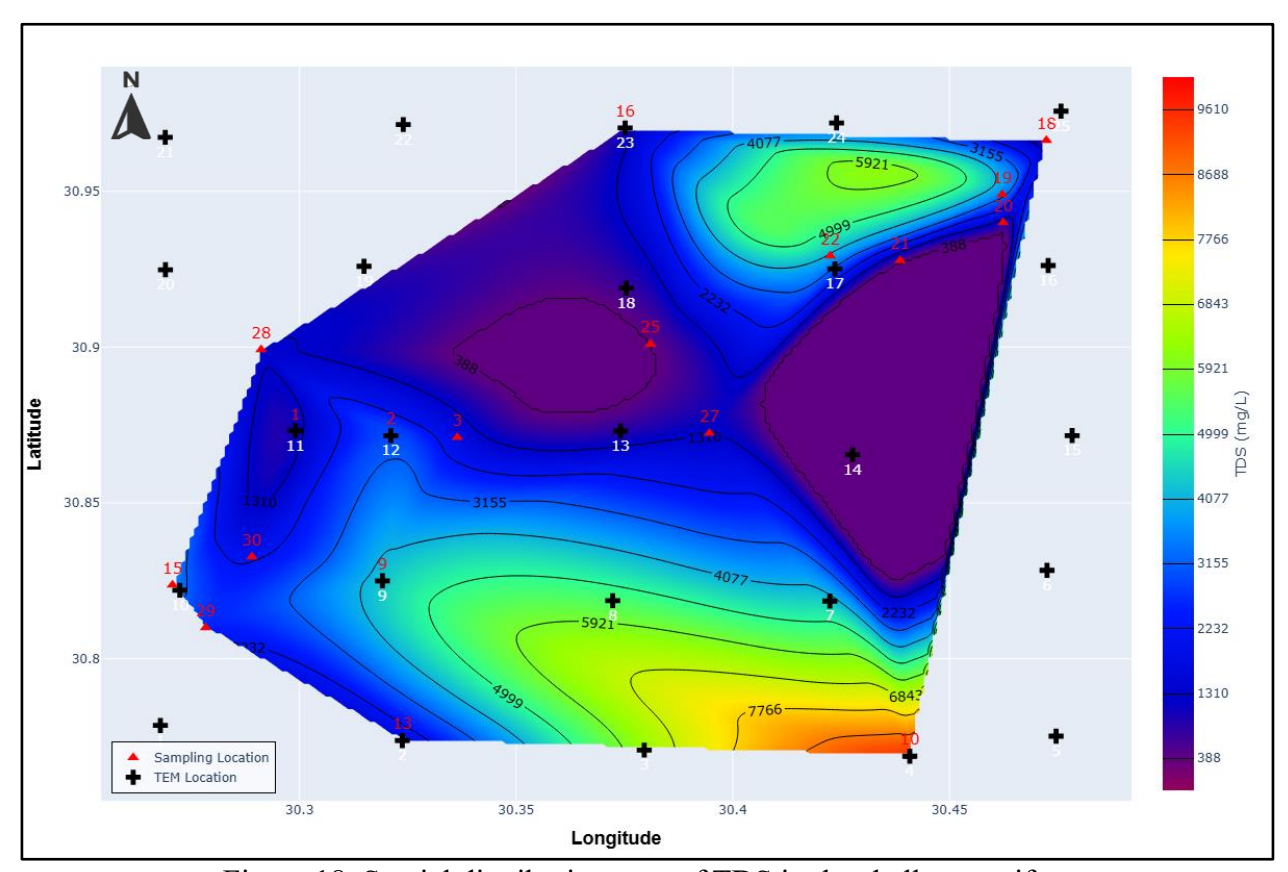


Figure 18. Spatial distribution map of TDS in the shallow aquifer.

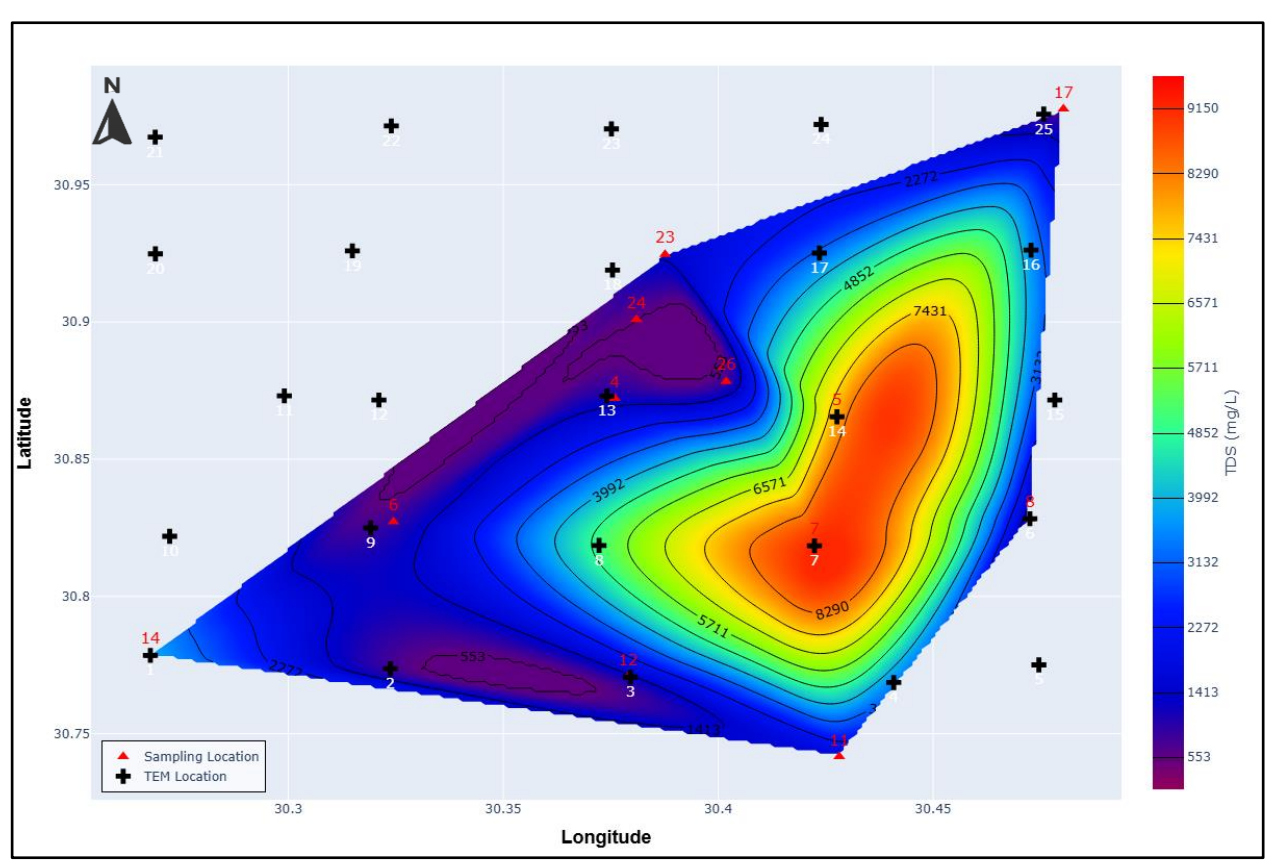


Figure 19. spatial distribution map of the TDS in the main aquifer.

# 3.2.3 Temporal and Spatial Evolution of Groundwater Quality (2012–2023)

Groundwater salinity has intensified notably between 2012 (Salem and Osman 2016, 2019) and the present study (2023), exhibiting a distinct north–south gradient (Table 2).

In the northern sector, both the shallow and main aquifers have experienced severe degradation because of progressive seawater intrusion. TDS values, which previously ranged from 650–1,870 mg/L in 2012, in 2023 reach up to 9,610 mg/L in the shallow aquifer, while in the main aquifer, they have risen from 549–2,450 mg/L to 1,292–9,150 mg/L. Similarly, chloride concentrations increased from 127.8–497 mg/L in 2012 to 20–3,900 mg/L in 2023 in the shallow aquifer, and from 52–887.5 mg/L to 63–3,000.2 mg/L in the main aquifer, confirming catastrophic salinization and deep penetration of marine water into both systems.

The central sector functions as a transitional mixing zone where both aquifers exhibit clear hydrochemical evolution over time. In the shallow aquifer, TDS increased from 690–1,007 mg/L in 2012 to 388–2,530 mg/L in 2023, indicating intensified irrigation return flow, fertilizer leaching, and partial saline mixing. In contrast, the main aquifer shows a slight decline in both TDS (from 1,085–2,450 to 914–1,292 mg/L) and chloride (from 149–887.5 to 50–180 mg/L), suggesting partial dilution by downward and lateral recharge of less mineralized water

from adjacent zones. This dilution is further supported by the spatial distribution of TDS (Figure 23), where relatively low values in the central area coincide with high nitrate concentrations, confirming that the recharge water is agriculture-derived rather than naturally fresh. The elevated NO<sub>3</sub><sup>-</sup> levels observed in 2023 thus indicate enhanced infiltration of polluted irrigation water, which reduces overall TDS and chloride temporarily but increases anthropogenic contamination.

In contrast, the southern sector remains comparatively buffered, maintaining TDS <1,500 mg/L in both aquifers. However, the observed increase in chloride concentrations, from 63.9–440 mg/L in 2012 to 20–455 mg/L in 2023 in the shallow aquifer, and from 131–198.8 mg/L to 50–600 mg/L in the main aquifer, indicates incipient salinization driven by pressure from the northward saline front and evaporative concentration under arid conditions.

Sector	Aquifer	2012 Wells	2023 Wells	TDS 2012 (mg/L)	TDS 2023 (mg/L)	Cl <sup>-</sup> 2012 (mg/L)	Cl <sup>-</sup> 2023 (mg/L)
North	Shallow	W46, W44	W16, W18, W21, W22, W20	650–1,870	1,029– 9,610	127.8–497	20–3,900
	Deep	W48, W54, W59, W60	W17, W23, W24	549–2,450	1,292– 9,150	52-887.5	63-3,000.2
Central		W33, W2	W27, W25, W2, W3, W1, W28	690–1,007	388–2,530	78.1–142	41–503
	Deep	W31, W48	W8, W4, W26	1,085– 2,450	914–1,292	149.1– 887.5	50–180
South	Shallow	W15, W56	W10, W13, W29, W15, W30	630–2,500	400–1,300	63.9–440	20–455
	Deep	W13, W68	W5, W6, W7, W11, W12, W14	733–780	553–1,496	131–198.8	50-600

Table 2. Temporal evolution of groundwater salinity (2012 vs. 2023).

# 3.3 Hydrochemical Facies

# 3.3.1 Piper Diagram

The hydrochemical facies of the groundwater were identified using the Piper trilinear diagram(Piper 1944), which integrates the relative concentrations of major cations and anions. A total of 30 groundwater samples from both shallow and main aquifers were plotted (**Figure 20**). Most samples fall into mixed zones where no single ion exceeds 50%, indicating heterogeneous water—rock interaction. Three dominant facies were recognized: **Na—HCO<sub>3</sub>**, reflecting cation exchange and silicate weathering; **Ca—SO<sub>4</sub>**, indicating evaporite dissolution; and **Na—Cl**, diagnostic of seawater intrusion. This facies distribution aligns with the observed spatial salinity gradients, where fresher waters in the central and southern areas contrast with intrusion-affected waters in the north.

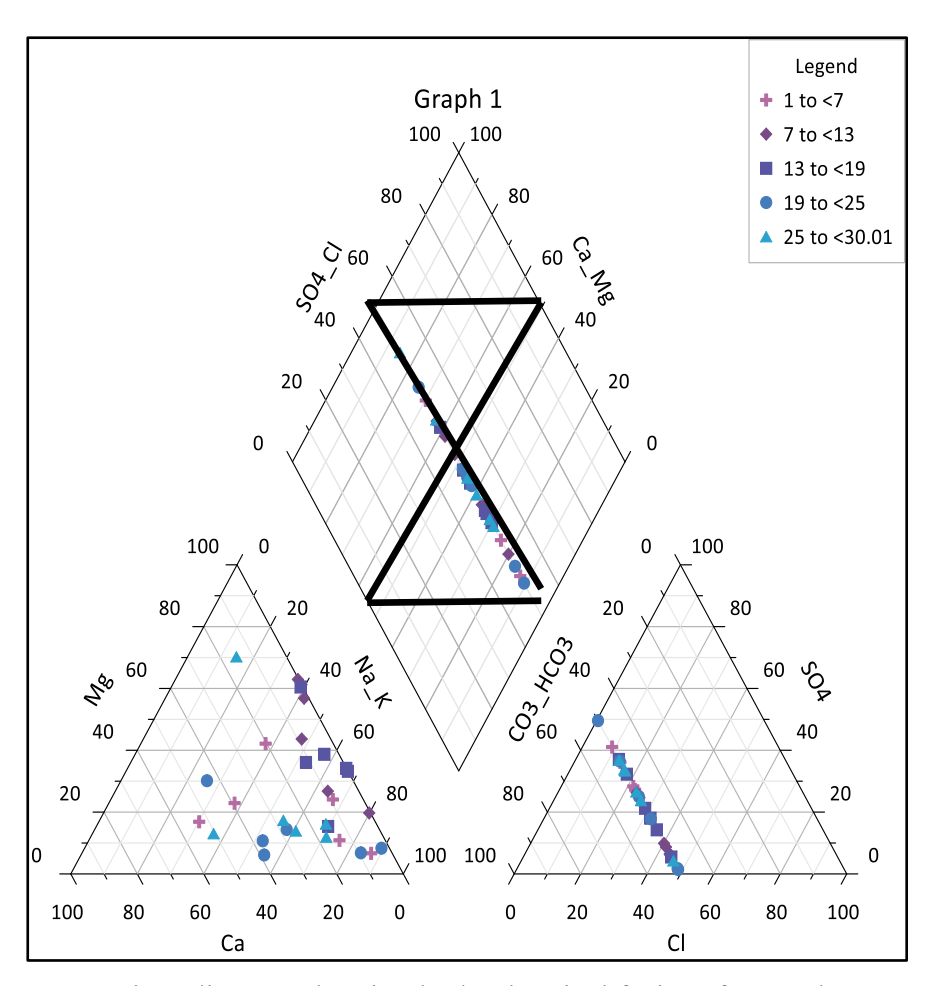
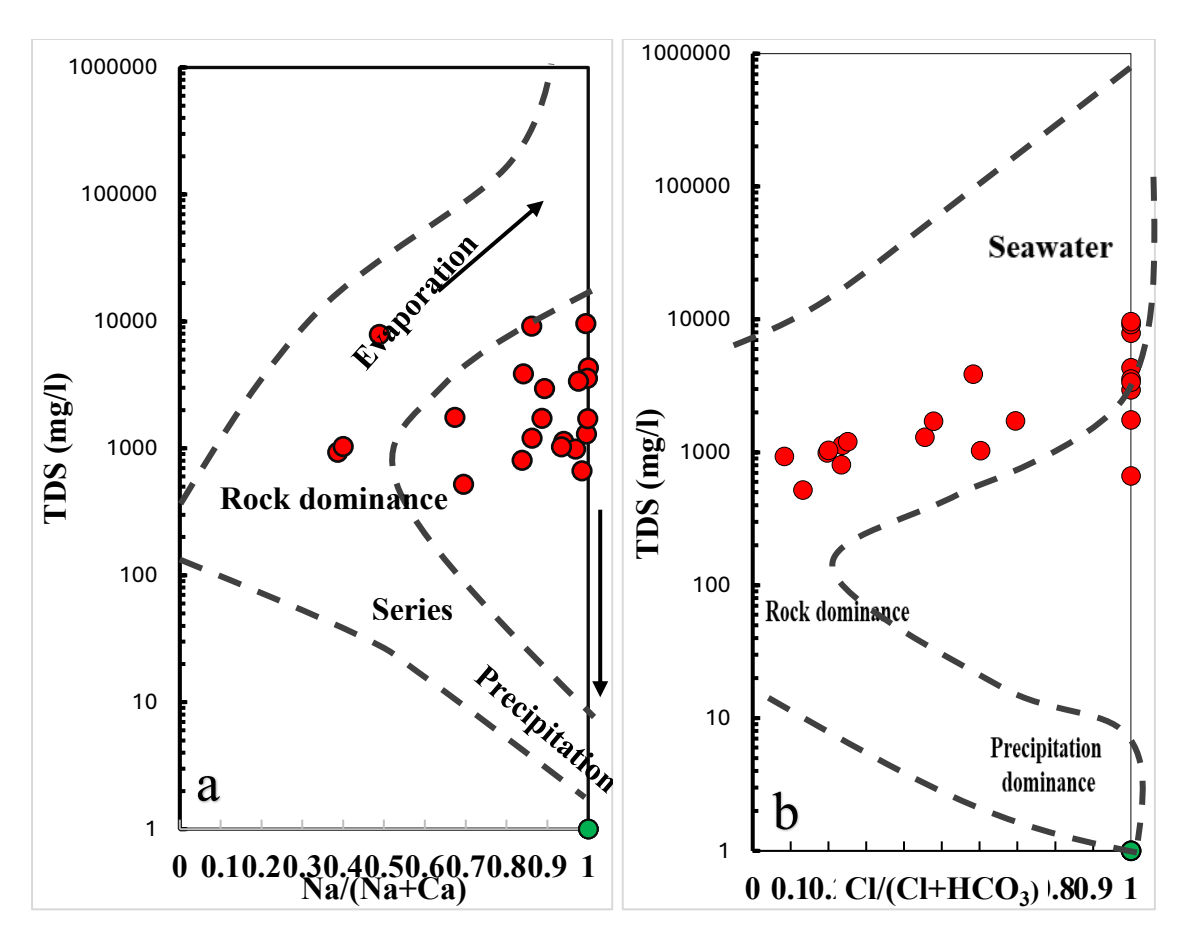


Figure 20. Piper diagram showing hydrochemical facies of groundwater samples from the shallow and main aquifers.

## 3.3.2 Gibbs Diagram

The Gibbs diagrams (Figure 21a, b) illustrate the principal mechanisms controlling groundwater chemistry in the study area. Most samples plot within the rock dominance and evaporation dominance fields, indicating that water–rock interaction, evaporative concentration, and mixing with saline water are the major geochemical processes influencing salinity. In Figure 21a, the progressive increase in Na<sup>+</sup>/(Na<sup>+</sup> + Ca<sup>2+</sup>) ratios with rising TDS suggests cation exchange reactions and sodium enrichment as salinity intensifies. Meanwhile, Figure 21b shows an increase in Cl<sup>-</sup>/(Cl<sup>-</sup> + HCO<sub>3</sub><sup>-</sup>) ratios with TDS, reflecting the growing impact of evaporation and chloride accumulation, typical of groundwater affected by seawater intrusion or evaporation-driven concentration. A few samples fall between the rock and evaporation dominance fields, signifying the combined effects of irrigation return flow and anthropogenic contamination, particularly the nitrate-enriched waters identified in the hydrochemical analysis. Overall, the Gibbs plots confirm that natural water–rock interaction, evaporation, and human-induced salinization jointly control the chemical evolution of groundwater in the study area.



**Figure 21.** Gibbs diagrams illustrating the mechanisms controlling groundwater chemistry: (a) plot of  $Na^+/(Na^+ + Ca^{2+})$  vs. TDS; (b) plot of  $Cl^-/(Cl^- + HCO_3^-)$  vs. TDS.

## 3.4 Drinking Water Quality (WQI)

The WQI results reveal a pronounced north—south gradient, with the northern aquifers classified as the most degraded due to seawater intrusion, high TDS, and chloride. The central sector shows further deterioration from agricultural activities, where nitrate pollution and leakage through shallow layers dominate. In contrast, the southern aquifers retain the best quality, benefiting from active recharge that dilutes salinity, though some wells already indicate early signs of encroaching salinization.

	Aquifer	Sector	Wells	WQI Range	Main Limiting Factors	Irrigation Suitability (Na%, SAR, MH, Cl <sup>-</sup> , etc.)
	Shallow	North	W16, W18, W21, W22, W20	374–2435	Seawater intrusion, very high TDS & Cl <sup>-</sup>	Na% up to 50%, Cl <sup>-</sup> up to 3900 mg/L, SAR 1–12
		Central	W1, W2, W3, W25, W28	55–635	Nitrate pollution (NO <sub>3</sub> <sup>-</sup> up to 948 mg/L), leakage	Na% 25–70%, SAR 2–16, Cl $^{\!-}$ up to 500 mg/L
		South	W10, W13, W15, W29, W30	23–230	Recharge influence, moderate salinity	Na% 50–85%, Cl <sup>-</sup> 455–1500 mg/L, SAR 3–17
	Main	North	W17, W23, W24	635–1946	Seawater intrusion, Cl <sup>-</sup> >3000 mg/L	Na% 13–45%, SAR up to 11, Cl $^{-}$ up to 3000 mg/L
		Central	W4, W8, W18, W19, W26	180–635	Moderate salinity, $NO_3^-$ leakage (up to 245 mg/L)	Na% 20–65%, SAR 1.5–15, Cl $^{\!-}$ up to 600 mg/L
		South	W5, W6, W7, W11, W12, W14	17–230	Recharge zones, early salinization	Na% 55–88%, SAR 4–17, Cl $^{\!-}$ up to 1200 mg/L

Table 3. Integrated Drinking and Irrigation Water Quality Assessment

## 3.5 Irrigation Water Quality

Groundwater suitability for irrigation follows a north–south gradient of improvement, mirroring the salinity distribution. In the northern sector, both aquifers are largely unsuitable due to excessive SAR, MH, PI, and chloride, which threaten soil structure and crop health. The central sector shows moderate to poor quality, where shallow wells are most affected by sodium and chloride hazards, while the main aquifer is slightly better but still limited by agricultural recharge and vertical leakage. The southern sector provides the most favorable conditions, generally falling within good to permissible classes, though some wells show elevated Na% and chloride that could restrict use for salt-sensitive crops.

#### 5. Discussion

Integrating TDEM, hydrochemical, and temporal datasets provides a coherent understanding of groundwater degradation across the study area. The combined results show a clear intensification of salinity both laterally and vertically over time, forming a north–south gradient that aligns with regional groundwater flow and subsurface structural control.

In the northern sector, the TDEM profiles reveal a deep and highly conductive zone (<1  $\Omega$ ·m) that corresponds to extremely high TDS (>9,000 mg/L) and chloride (>3,000 mg/L) in both aquifers (Figures 22 and 23). This confirms the presence of a severe seawater intrusion plume that has penetrated deeply into the main aquifer, reducing the thickness of the freshwater zone and indicating intrusion along permeable structural pathways. The 3D resistivity model (Figure 21) further shows that the main aquifer is increasingly overlain and laterally confined by low-resistivity clay-rich units. These clay bodies do not generate salinity but restrict natural flushing and limit freshwater recharge, allowing the intruded saline water to persist and intensify. However, the relatively wide spacing used in the TDEM survey ( $\sim$ 5,000 m) limits the resolution of thin clay interlayers and narrow fractures that may act as preferential pathways for saline migration (Abdalsalam, 2025; Olorunfemi et al., 2005). Thus, finer-scale conduits of intrusion may remain undetected without denser geophysical coverage.

In the central sector, the TDEM sections exhibit moderate resistivity values representing a well-developed shallow aquifer underlain by a thin or discontinuous confining clay layer. This weak hydraulic separation allows upward migration of saline water from the main aquifer and downward infiltration of agricultural return flow, creating a hydrogeological mixing zone. Elevated nitrate concentrations (up to 914 mg/L) reflect fertilizer leaching and irrigation recharge, while increased chloride and TDS (~2,500 mg/L) indicate partial mixing with saline water. Temporal comparison shows that the shallow aquifer has increased salinization (TDS from 690–1,007 mg/L to 388–2,530 mg/L), whereas the main aquifer shows slight decreases in TDS (1,085–2,450 to 914–1,292 mg/L) and chloride (149–887.5 to 50–180 mg/L), indicating partial dilution by lateral or downward movement of less-mineralized recharge. The spatial TDS patterns (Figure 23) support this interpretation, as lower TDS in the central zone coincides with higher NO<sub>3</sub>-, confirming the recharge source is agriculture-derived rather than naturally fresh. This represents a hydrogeological trade-off: temporary dilution of salinity accompanied by long-term deterioration due to nitrate contamination. The increasing similarity of shallow and deep water chemistry confirms vertical hydraulic connectivity

through fractured and semi-confining layers. Thus, the central sector is the most hydrodynamically active and vulnerable zone where saline and polluted waters converge and enhance inland salinity migration.

The southern sector retains the freshest groundwater, characterized by high resistivity (>25  $\Omega$ ·m), low TDS (<1,500 mg/L), and relatively low chloride (<600 mg/L), indicating active recharge and coarser sandy layers. Only slight increases in chloride and sulfate are observed compared with 2012, suggesting the initial stage of advancement in salinity toward this zone. A modest decline in resistivity near the margins supports this early shift, implying the southern aquifer, although still the least degraded, is beginning to respond to hydraulic pressure from the expanding saline front.

Hydrochemical facies classification using the Piper diagram (Figure 24) identifies Na–Cl waters associated with seawater intrusion, Ca–SO<sub>4</sub> waters linked to evaporite dissolution and irrigation return flow, and Na–HCO<sub>3</sub> waters reflecting natural silicate weathering in recharge zones. The Gibbs diagrams (Figure 25) indicate that groundwater chemistry is controlled by a combination of rock–water interaction, evaporation, and anthropogenic influence. Water quality indices (WQI, Na%, SAR, MH, Cl<sup>-</sup>) show that northern and central waters are largely unsuitable for drinking and irrigation, whereas southern wells fall within the good to permissible categories but still require management to prevent further deterioration.

Overall, groundwater degradation in the study area is driven by seawater intrusion, vertical leakage, and agricultural contamination, each controlled by subsurface lithology and hydraulic structure. Subsurface resistivity patterns strongly mirror salinity distribution, confirming an inverse relationship between resistivity and TDS. Together, these findings underscore the need for zone-specific management and targeted monitoring.

## 6. Recommendations

- 1. Northern Sector (Intrusion Control):
  - o Reduce groundwater abstraction rates.
  - o Evaluate hydraulic barriers or artificial recharge wells to slow saline advancement.
- 2. Central Sector (Pollution & Leakage Control):
  - o Regulate fertilizer and irrigation practices to reduce nitrate leaching.
  - o Prevent excavation or drilling that further disrupts confining layers.

## 3. Southern Sector (Resource Protection):

- o Establish groundwater protection zones and restrict high-capacity well installation.
- o Implement artificial recharge using treated low-salinity water.

## 4. Monitoring and Future Work:

- o Conduct denser geophysical surveys and integrate TDEM with ERT and borehole logging to resolve fine mixing pathways.
- o Establish continuous monitoring of TDS, Cl⁻, and NO₃⁻ in both aquifers.

#### 6. Conclusion

This study demonstrates that integrating time-domain electromagnetic (TDEM) data with hydrochemical analyses and temporal comparisons provides a powerful approach for diagnosing groundwater degradation processes across the western Nile Delta. The results reveal that groundwater salinity has intensified laterally and vertically over time, forming a distinct north—south gradient that mirrors regional groundwater flow and structural control.

In the northern sector, severe seawater intrusion has deeply penetrated the main aquifer through permeable structural pathways, leading to extremely low resistivity and high salinity values. The central sector represents a dynamic mixing zone where upward saline leakage and downward infiltration of agricultural return flow coexist, producing a complex interaction between salinity dilution and nitrate contamination. The southern sector still retains relatively fresh groundwater, yet early signs of salinization indicate that the saline front is gradually advancing inland.

Hydrochemical facies and Gibbs diagram interpretations confirm that groundwater chemistry is influenced by a combination of seawater mixing, rock—water interaction, evaporation, and anthropogenic inputs. The inverse relationship between resistivity and TDS highlights the strong diagnostic capability of TDEM in mapping salinity variations and identifying areas of hydraulic connectivity.

The integrated methodological framework presented in this study offers a replicable model for other coastal aquifers facing similar challenges of salinization and contamination under increasing anthropogenic and climatic pressures.

#### 7 References

- Abd El-Fattah BK, Moustafa AR, Yousef M (2021) A new insight into the structural evolution of Rosetta Fault, eastern margin of Herodotus Basin, East Mediterranean.

  Mar Pet Geol 131:105161. https://doi.org/10.1016/j.marpetgeo.2021.105161
- Abd-Allah AMA, Abdel Aal MH, Ghandour A (2012) Structural characteristics and tectonic evolution of the northwestern margin of the Nile Delta, Egypt. Journal of African Earth Sciences 68:82–95. https://doi.org/10.1016/j.jafrearsci.2012.02.006
- Abdalsalam A, A.Tarabees E, Abdelrahman K, et al (2025) Integrating electromagnetic methods to identify the groundwater-bearing zones, a case study of the New Nubariya city in the northwestern of Egypt. All Earth 37:1–23. https://doi.org/10.1080/27669645.2025.2555076
- Abdel Baki AA (1983) Hydrogeological and hydrochemical studies on the area west of Rosette branch and south of El-Nasr Canal. Fac. Sci., Ain Shams Univ., Cairo, Egypt
- Abdel Dayem AA (1976) Meloration hydrogeology in west El-Nubaria area. Fac. Sci. El-Mansoura Univ., Egypt
- Abdel Wahab S (1999) Hydrogeological and isotope assessment of groundwater in Wadi El-Natrum and Sadat city, Egypt. Fac. Sci. Ain Shams Univ. Egypt
- Aboukota MES, Hassaballa H, Elhini M, Ganzour SK (2024) Land Degradation,
  Desertification & Environmental Sensitivity to Climate Change in Alexandria and
  Beheira, Egypt. Egyptian Journal of Soil Science 64:167–180.
  https://doi.org/10.21608/ejss.2023.237386.1664
- Abuzaid AG, Sabet HS, Al (2024) temamy. A M M Estimating Geophysical and Hydrogeological Parameters through Well Logging and Hydrogeological Data in El-Sadat City Extension, West Nile Delta, Egypt Egyptian Journal of Geology 68:277–288. https://doi.org/10.21608/egig.2024.310607.1085
- Ali K, Ebrahem O, Zayed M (2024) Assessment of groundwater resources to support urban extension in West Nile Delta, Egypt. Arabian Journal of Geosciences 17:1–20. https://doi.org/10.1007/s12517-024-12121-0
- Alzahrani H, Basaloom A, Mosaad S (2025) Geochemical-based appraisal of karst groundwater quality, west Nile Valley, central Egypt, for drinking and irrigation. J Hydrol Reg Stud 57:102152. https://doi.org/10.1016/j.ejrh.2024.102152
- Amiri V, Ali S, Sohrabi N, Amiri F (2023) Hydrogeochemical evaluation with emphasis on nitrate and fluoride in urban and rural drinking water resources in western Isfahan

- province, central Iran. Environmental Science and Pollution Research 30:108720–108740. https://doi.org/10.1007/s11356-023-30001-0
- (APHA) APHA (2017) Standard methods for the examination of water and wastewater (23rd ed.). APHA, Washington, DC
- Araffa SAS, Abdulattif A, Al Deep M, et al (2025) Integrated geophysical and hydrochemical assessment of groundwater aquifers for agricultural development: a case study in the Area South Alamein-Wadi El Natrun Road, Egypt. All Earth 37:1–17. https://doi.org/10.1080/27669645.2025.2463735
- Araffa SAS, Soliman AS (2019) El Khafif, A., Younis, A., Shazley. T Environmental investigation using geophysical data at East Sadat City, Egypt Egyptian Journal of Petroleum 28:117–125. https://doi.org/10.1016/j.ejpe.2018.12.002
- Archie GE (1942) The electrical resistivity log as an aid in determining some reservoir characteristics. Transactions of the AIME 146:54–62. https://doi.org/10.2118/942054-G
- Awad M, Mohamed E, Saber S, et al (2022) Hydrogeochemical studies of the groundwater at the flood plain Quaternary aquifer in Beni suef area, Egypt. Egyptian Journal of Chemistry, 0(0). https://doi.org/10.21608/ejchem.2022.132791.5877
- Awad MA, El-Arabi NE, Hamza MS (1997) Use of solute chemistry and isotopes to identify sources of groundwater recharge in Nile aquifer system, Upper Egypt. Magazine of ``GROUNDWATER''. America (NY) 35:1997
- CONOCO (1987) Geological Maps of Egypt Scale 1:500,000. Sheet Nos. NG 36 NW Cairo. The Egyptian General Petroleum Corporation, Egypt
- Constable SC, Parker RL, Constable CG (1987) Occam's inversion: A practical algorithm for generating smooth models from electromagnetic sounding data. Geophysics 52:289–300. https://doi.org/10.1190/1.1442303
- El Bastawesy M, Cherif OH, Sultan M (2016) The geomorphological evidences of subsidence in the Nile Delta: Analysis of high resolution topographic DEM and multi-temporal satellite images. Journal of African Earth Sciences 136:252–261. https://doi.org/10.1016/j.jafrearsci.2016.10.013
- El Fayoumy IF (1964) Geology of groundwater supplies in Wadi El-Natrun area. Fac. Sci. Cairo Univ., Egypt
- El Ghazawi MM (1982) Geological studies of the Quaternary-Neogene aquifers in the area northwest Nile Delta. Al-Azhar Univ., Cairo, Egypt

- El Osta M, Masoud M, Badran O (2021) Aquifer hydraulic parameters estimation based on hydrogeophysical methods in West Nile Delta, Egypt. Environ Earth Sci 80:344. https://doi.org/10.1007/s12665-021-09617-3
- El Shazly EM, Abdel-Hady M, El Ghawaby MA, et al (1975) Geologic interpretation of Landsat satellite images for west Nile delta area, Egypt. Remote Sensing Research Project, Academy of Scientific Research Technology, Cairo 1977:479–544
- El-Agha DE, Molle F, Metwally MI, et al (2024) Toward sustainable management of groundwater in the deserts of Egypt. Hydrogeol J 32:663–678. https://doi.org/10.1007/s10040-023-02738-y
- Elbeih S, Zaghloul E, Hagage M, et al (2025) Groundwater Mapping of the New Delta Area (West of Nile Delta) Using Geographic Information Systems and Satellite Images. In: Groundwater in Developing Countries. Springer Nature Switzerland, Cham, pp 217–230
- El-Hassanin AS, Abdallah SA, Saleh NM, Abou Kota MS (2016) ADVANCES IN SOIL SALINITY DETECTION IN ARID AND SEMI- ARID REGIONS USING SALINITY AND VEGETATION INDICES. Menoufia Journal of Soil Science 1:65–75. https://doi.org/10.21608/mjss.2016.176588
- ElMahmoudi A, Shalaby A, Aboelkhair H, Rashad E (2020) Evaluation of the Groundwater Quality of the Miocene Aquifer and its suitability for Domestic and Agriculture Purposes, West Nile Delta, Egypt. Scientific Journal for Damietta Faculty of Science 10:80–87. https://doi.org/10.21608/sjdfs.2020.195002
- Embaby AA (2003) Environment Evaluation for Geomorphological Situation in relation to the water and soil resources of the region north of the Sadat city, west Nile Delta, Egypt. Fac. Sci. Damietta, Mansoura Univ., Cairo, Egypt
- Fattah M kamel (2017) Evaluation of Water Resources in Wadi El Natrun, Western Desert, Egypt. International Journal of Environment, Agriculture and Biotechnology 2:329–349. https://doi.org/10.22161/ijeab/2.1.42
- Fitterman D V, Stewart MT (1986) Transient electromagnetic sounding for groundwater. Geophysics 51:995–1005. https://doi.org/10.1190/1.1442158
- Francés AP, Ramalho EC, Monteiro Santos F, et al (2024) Contribution of the time domain electromagnetic method to the study of the Kalahari transboundary multilayered aquifer systems in Southern Angola. Hydrogeol J 32:1709–1727. https://doi.org/10.1007/s10040-024-02822-x
- Freeze RA, Cherry JA (1979) Groundwater. Prentice-Hall, Englewood Cliffs, New Jersey

- Gad M, El Hattab M, Galal S (2016) Assessment of the Miocene aquifer in Wadi El Farigh area by using GIS techniques. NRIAG Journal of Astronomy and Geophysics 5:463–473. https://doi.org/10.1016/j.nrjag.2016.11.001
- Gibbs RJ (1970) Mechanisms controlling world water chemistry. Science (1979) 170:1088–1090
- Hasan SS, Salem ZE, Sefelnasr A (2023) Assessment of Hydrogeochemical Characteristics and Seawater Intrusion in Coastal Aquifers by Integrating Statistical and Graphical Techniques: Quaternary Aquifer, West Nile Delta, Egypt. Water (Basel) 15:1803. https://doi.org/10.3390/w15101803
- Hefny K, El Gandour MFM, Khalil JB, Atta SA (1991) Groundwater
- Hegarty A, Stanley G, Kashdan E, et al (2016) Repeatability analysis of airborne electromagnetic surveys. Math Ind Case Stud 7:. https://doi.org/10.1186/s40929-016-0008-1
- Hem JD (1985) Study and interpretation of the chemical characteristics of the natural water, 3rd edn. U. S. Geological survey, Water supply paper 2254
- Ibraheem IM, El-Qady GM, ElGalladi A (2016) Hydrogeophysical and structural investigation using VES and TDEM data: A case study at El-Nubariya–Wadi El-Natrun area, west Nile Delta, Egypt. NRIAG Journal of Astronomy and Geophysics 5:198–215. https://doi.org/10.1016/j.nrjag.2016.04.004
- Ibraheem IM, Othman A, Ghazala H (2022) Pliocene aquifer characterization using TEM and VES geophysical techniques: case study at the area to the east of Wadi El-Natrun City, West Nile Delta, Egypt. In: Sustainability of Groundwater in the Nile Valley, Egypt. Springer International Publishing, Cham, pp 235–266
- Institute D (1974) Report on the regional hydrogeological studies of the West El Nubaria area (300,000 Feddans reclamation project), internal report, Cairo, Egypt
- Joshi DM, Kumar A, Agrawal N, Singh V (2009) Assessment of the irrigation water quality of River Ganga in Haridwar District. Rasayan Journal of Chemistry 2:285–292
- Keller G V, Kaufman AA (1983) Transient electromagnetic soundings: An integrated approach. J Struct Geol 6:283–291. https://doi.org/10.1111/j.1365-246X.1984.tb02230.x
- Kellner A, Brink GJ, El Khawaga H (2018) Depositional history of the western Nile Delta, Egypt: Late Rupelian to Pleistocene. Am Assoc Pet Geol Bull 102:1841–1865. https://doi.org/10.1306/02161817234
- Khaled MA, Youssef AM, Barseem MS (2017) STRUCTURAL IMPACT OF THE TERTIARY BASALT SETTING ON THE GROUNDWATER AQUIFERS USING GEOPHYSICAL

- TECHNIQUES IN THE AREA WEST CAIRO-ALEX. DESERT HIGHWAY BETWEEN THE KM 42 AND 52. Journal of Egyptian Geophysical Society 15:19–37. https://doi.org/10.21608/jegs.2017.385674
- Khalifa M, Gemail K (2025) Geology of the Nile Deltas and Natural Resources: Challenges and Sustainable Management. Springer, Cham
- Khalil A, Mansour K, Rabeh T, et al (2014) Geophysical Evaluation for Evidence of Recharging the Pleistocene Aquifer at El-Nubariya Area, West Nile Delta, Egypt. International Journal of Geosciences 5:324–340. https://doi.org/10.4236/ijg.2014.53032
- Kotb THS, Watanabe T, Ogino Y, Tanji KK (2000) Soil salinization in the Nile Delta and related policy issues in Egypt. Agric Water Manag 43:239–261. https://doi.org/10.1016/s0378-3774(99)00052-9
- Krivochieva S, Chouteau M (2003) Integrating TDEM and MT methods for characterization and delineation of the Santa Catarina aquifer (Chalco Sub-Basin, Mexico). J Appl Geophy 52:23–43. https://doi.org/10.1016/S0926-9851(02)00231-8
- Kumar A, Maurya NS (2023) Groundwater quality assessment using the WQI and GIS mapping: suitability for drinking and irrigation usage in the Sirdala block of Nawada district. Water Supply
- Machado MA (2024) Eddy Currents Probe Design for NDT Applications: A Review. Sensors 24:5819. https://doi.org/10.3390/s24175819
- Mansour K, Gomaa M, Taha AI, et al (2023) Investigation of Groundwater Occurrences Along the Nile Valley Between South Cairo and Beni Suef, Egypt, Using Geophysical and Geodetic Techniques. Pure Appl Geophys 180:3071–3088. https://doi.org/10.1007/s00024-023-03306-x
- Mashaal N, Akagi T, Ishibashi J (2020) Hydrochemical and isotopic study of groundwater in Wadi El-Natrun, Western Desert, Egypt: Implication for salinization processes.

  Journal of African Earth Sciences 172:104011.

  https://doi.org/10.1016/j.jafrearsci.2020.104011
- Mohammed AM, Refaee A, El-Din GK, Harb S (2022) Hydrochemical characteristics and quality assessment of shallow groundwater under intensive agriculture practices in arid region, Qena, Egypt. Appl Water Sci 12:. https://doi.org/10.1007/s13201-022-01611-9
- Moursy AR, Elsayed MA, Fadl ME, Abdalazem AH (2025) PRISMA-Driven Hyperspectral Analysis for characterization of Soil Salinity Patterns in Sohag, Egypt. Egyptian Journal of Soil Science 65:15–31. https://doi.org/10.21608/ejss.2024.310679.1836

- Nabighian MN, Macnae JC (1991) Time-domain electromagnetic theory for geophysical applications. In: Nabighian MN (ed) Electromagnetic Methods in Applied Geophysics. Society of Exploration Geophysicists, pp 427–520
- Nabighian MN, Macnae JC (1988) Time Domain Electromagnetic Prospecting
- Negm AM, Sakr S, Abd-Elaty I, Abd-Elhamid HF (2018) An overview of groundwater resources in Nile Delta aquifer. Groundwater in the Nile delta 3–44. https://doi.org/10.1007/698\_2017\_193
- Nosair AM, Shehata M, Ehab Zaghlool ZM, et al (2025) Integration of hydrogeochemical, isotopic, remote sensing and machine learning to assess seawater intrusion in an arid coastal aquifer, Sudr area, South Sinai, Egypt. Model Earth Syst Environ 11:. https://doi.org/10.1007/s40808-025-02499-5
- Omara SM, Sanad S (1975) Rock stratigraphy and structural features of the area between Wadi El-Natrun and Moghra depression, western desert, Egypt. Geol Jb 1:45–73
- Othman A, Ibraheem IM, Ghazala H, et al (2019) Hydrogeophysical and hydrochemical characteristics of Pliocene groundwater aquifer at the area northwest El Sadat city, West Nile Delta, Egypt. Journal of African Earth Sciences 150:1–11. https://doi.org/10.1016/j.jafrearsci.2018.10.011
- Pennington BT, Sturt F, Wilson P, et al (2017) The fluvial evolution of the Holocene Nile Delta. Quat Sci Rev 170:212–231. https://doi.org/10.1016/j.quascirev.2017.06.017
- Piper AM (1944) A graphic procedure in the geochemical interpretation of water analyses. Transactions of the American Geophysical Union 25:914–928
- Said R (1962) Geology of Egypt. Elsevier Publishing Co, Amsterdam, New York
- Saleh S (2012) The role of geophysical and seismological data in evaluating the subsurface structures and tectonic trends of Nile Delta, Egypt. Arabian Journal of Geosciences 6:3201–3216. https://doi.org/10.1007/s12517-012-0603-9
- Salem ZE, El-Bayumy DA (2016) Hydrogeological, petrophysical and hydrogeochemical characteristics of the groundwater aquifers east of Wadi El-Natrun, Egypt. NRIAG Journal of Astronomy and Geophysics 5:124–146. https://doi.org/10.1016/j.nrjag.2015.12.001
- Salem ZE, Osman OM (2019) Use of geoelectrical resistivity to delineate the seawater intrusion in the northwestern part of the Nile Delta, Egypt. Groundwater in the Nile Delta 425–459
- Salem ZE-S, Osman OM (2016) Use of major ions to evaluate the hydrogeochemistry of groundwater influenced by reclamation and seawater intrusion, West Nile Delta,

- Egypt. Environmental Science and Pollution Research 24:3675–3704. https://doi.org/10.1007/s11356-016-8056-4
- Sallouma MK, Gomaa MA (1997) Groundwater quality in the Miocene aquifer east and west of Nile Delta and in the north of the Western Desert, Egypt. Ain Shams Sci Bull 35:47–72
- Sandford KS, Arkell WJ (1939) Paleolithic Man and Nile Valley in Lower Egypt. Oriental Institute Publications, Chicago, IL
- Shalaby A, Sarhan MA (2023) Pre-and post-Messinian deformational styles along the northern Nile Delta Basin in the framework of the Eastern Mediterranean tectonic evolution. Marine Geophysical Research 44:22. https://doi.org/10.1007/s11001-023-09530-3
- Shankar K, Nagaraju A, Rao TG, Rao SM (2018) Hydrogeochemical evaluation of groundwater quality for drinking and irrigation purposes, Vemula area, Kadapa District, Andhra Pradesh, India. Appl Water Sci 8:1
- Sharaky AM, Saleh N, Farok OM, Saadany ER (2021) Groundwater Quality and Potentiality of Moghra Aquifer, Northwestern Desert, Egypt. Springer Water 243–275. https://doi.org/10.1007/978-3-030-77622-0\_10
- Shata AA, El Fayoumy IF, Tamer M (1970) Geology, hydrogeology and soil of Wadi El-Natrun-Maryut agriculture project. Int. Rep, Desert Institute, Cairo, Egypt
- Shata AA, El Shazly MM, Attia SH, Aboul-Fetouh M (1978) The geology of the quaternary deposits and their natural relation to soil formations in the fringes west of the Nile Delta, Egypt. Desert Inst Bull, ARE 28:43–77
- Sherif MM, Singh VP (1997) Groundwater development and sustainability in the Nile Delta aquifer. Final Report, Binational Fulbright Commission, Egypt
- Shin S, Aziz D, El-sayed MEA, et al (2022) Systems Thinking for Planning Sustainable Desert Agriculture Systems with Saline Groundwater Irrigation: A Review. Water (Basel) 14:3343. https://doi.org/10.3390/w14203343
- Spies BR, Frischknecht FC (1991) Electromagnetic sounding
- USGS (1984) Earthshots, satellite images of Environmental change, Nile river Delta, Egypt; http://edcwww. Cr. USGS. Gov/earthshots/slow Nile/Nile
- Van Engelen J, Oude Essink GH, Kooi H, Bierkens MF (2018) On the origins of hypersaline groundwater in the Nile Delta aquifer. J Hydrol (Amst) 560:301–317
- Ward SH, Hohmann GW (1988) Electromagnetic Theory for Geophysical Applications. Society of Exploration Geophysicists

- (WHO) WHO (2011) Guidelines for Drinking-water Quality, 4th edn. World Health Organization, Geneva
- Williams WD (2001) Hydrobiologia. 466:329–337. https://doi.org/10.1023/a:1014598509028
- Wu J, Li P, Qian H, et al (2013) Using correlation and multivariate statistical analysis to identify hydrogeochemical processes affecting the major ion chemistry of waters: a case study in Laoheba phosphorite mine in Sichuan, China. Arabian Journal of Geosciences 7:3973–3982. https://doi.org/10.1007/s12517-013-1057-4
- Xing K, Li S, Qu Z, Zhang X (2024) Time-Domain Electromagnetic Noise Suppression Using Multivariate Variational Mode Decomposition. Remote Sens (Basel) 16:806. https://doi.org/10.3390/rs16050806
- Zaghloul EA (2013) Physical geology and historical settlement in Northwestern Nile
- Zaghloul EA, Abdeen MM, Elbeih SF, Soliman MA (2020) Water logging problems in Egypt's Deserts: Case study Abu Mena archaeological site using geospatial techniques. The Egyptian Journal of Remote Sensing and Space Science 23:387–399. https://doi.org/10.1016/j.ejrs.2020.06.003
- Zhang Z, Yao W, Huang Y, et al (2024) Irrigation Water Salinity Affects Solute Transport and Its Potential Factors Influencing Salt Distribution in Unsaturated Homogenous Red Soil. Agronomy 14:2453. https://doi.org/10.3390/agronomy14112453
- Zhdanov MS (2009) Methods in Geochemistry and Geophysics: Geophysical Electromagnetic Theory and Methods. Elsevier, Netherlands
- Zhdanov MS, Portniaguine O (1997) Time-domain electromagnetic migration in the solution of inverse problems. Geophys J Int 131:293–309. https://doi.org/10.1111/j.1365-246x.1997.tb01223.x
- Ziadi A, Hariga NT, Tarhouni J (2017) Use of time-domain electromagnetic (TDEM) method to investigate seawater intrusion in the Lebna coastal aquifer of eastern Cap Bon, Tunisia. Arabian Journal of Geosciences 10:. https://doi.org/10.1007/s12517-017-3265-9